

Search for evidence of compositeness at LEP I

The ALEPH Collaboration¹

Abstract

Extensive searches for evidence of compositeness of quarks and leptons have been made using the full set of ALEPH data from LEP running at the Z peak. They include searches for radiative and weak decays of excited leptons, and radiative and gluonic decays of excited quarks, produced either singly or in pairs. Searches have also been made for a scalar partner of the Z boson in all decay modes. No evidence for such states has been found and coupling and branching ratio limits are presented. Limits are also given for the branching ratios for $Z \rightarrow gg\gamma$ and $Z \rightarrow \gamma\gamma\gamma$.

To be submitted to *European Physical Journal C*

¹See following pages for list of authors.

The ALEPH Collaboration

R. Barate, D. Buskulic, D. Decamp, P. Ghez, C. Goy, J.-P. Lees, A. Lucotte, E. Merle, M.-N. Minard, J.-Y. Nief, B. Pietrzyk

Laboratoire de Physique des Particules (LAPP), IN²P³-CNRS, 74019 Annecy-le-Vieux Cedex, France

R. Alemany, G. Boix, M.P. Casado, M. Chmeissani, J.M. Crespo, M. Delfino, E. Fernandez, M. Fernandez-Bosman, Ll. Garrido,¹⁵ E. Graugès, A. Juste, M. Martinez, G. Merino, R. Miquel, Ll.M. Mir, I.C. Park, A. Pascual, J.A. Perlas, I. Riu, F. Sanchez

Institut de Física d'Altes Energies, Universitat Autònoma de Barcelona, 08193 Bellaterra (Barcelona), Spain⁷

A. Colaleo, D. Creanza, M. de Palma, G. Gelao, G. Iaselli, G. Maggi, M. Maggi, S. Nuzzo, A. Ranieri, G. Raso, F. Ruggieri, G. Selvaggi, L. Silvestris, P. Tempesta, A. Tricomi,³ G. Zito

Dipartimento di Fisica, INFN Sezione di Bari, 70126 Bari, Italy

X. Huang, J. Lin, Q. Ouyang, T. Wang, Y. Xie, R. Xu, S. Xue, J. Zhang, L. Zhang, W. Zhao

Institute of High-Energy Physics, Academia Sinica, Beijing, The People's Republic of China⁸

D. Abbaneo, U. Becker, P. Bright-Thomas, D. Casper, M. Cattaneo, V. Ciulli, G. Dissertori, H. Drevermann, R.W. Forty, M. Frank, R. Hagelberg, J.B. Hansen, J. Harvey, P. Janot, B. Jost, I. Lehraus, P. Mato, A. Minten, L. Moneta,²¹ A. Pacheco, J.-F. Puztaszeri,²³ F. Ranjard, L. Rolandi, D. Rousseau, D. Schlatter, M. Schmitt,²⁵ O. Schneider, W. Tejessy, F. Teubert, I.R. Tomalin, H. Wachsmuth, A. Wagner²⁰

European Laboratory for Particle Physics (CERN), 1211 Geneva 23, Switzerland

Z. Ajaltouni, F. Badaud, G. Chazelle, O. Deschamps, A. Falvard, C. Ferdi, P. Gay, C. Guicheney, P. Henrard, J. Jousset, B. Michel, S. Monteil, J-C. Montret, D. Pallin, P. Perret, F. Podlyski, J. Proriol, P. Rosnet

Laboratoire de Physique Corpusculaire, Université Blaise Pascal, IN²P³-CNRS, Clermont-Ferrand, 63177 Aubière, France

J.D. Hansen, J.R. Hansen, P.H. Hansen, B.S. Nilsson, B. Rensch, A. Wäänänen

Niels Bohr Institute, 2100 Copenhagen, Denmark⁹

G. Daskalakis, A. Kyriakis, C. Markou, E. Simopoulou, I. Siotis, A. Vayaki

Nuclear Research Center Demokritos (NRCD), Athens, Greece

A. Blondel, G. Bonneaud, J.-C. Brient, P. Bourdon, A. Rougé, M. Rumpf, A. Valassi,⁶ M. Verderi, H. Videau

Laboratoire de Physique Nucléaire et des Hautes Energies, Ecole Polytechnique, IN²P³-CNRS, 91128 Palaiseau Cedex, France

E. Focardi, G. Parrini, K. Zachariadou

Dipartimento di Fisica, Università di Firenze, INFN Sezione di Firenze, 50125 Firenze, Italy

M. Corden, C. Georgiopoulos, D.E. Jaffe

Supercomputer Computations Research Institute, Florida State University, Tallahassee, FL 32306-4052, USA^{13,14}

A. Antonelli, G. Bencivenni, G. Bologna,⁴ F. Bossi, P. Campana, G. Capon, F. Cerutti, V. Chiarella, G. Felici, P. Laurelli, G. Mannocchi,⁵ F. Murtas, G.P. Murtas, L. Passalacqua, M. Pepe-Altarelli

Laboratori Nazionali dell'INFN (LNF-INFN), 00044 Frascati, Italy

L. Curtis, A.W. Halley, J.G. Lynch, P. Negus, V. O'Shea, C. Raine, J.M. Scarr, K. Smith, P. Teixeira-Dias, A.S. Thompson, E. Thomson

Department of Physics and Astronomy, University of Glasgow, Glasgow G12 8QQ, United Kingdom¹⁰

O. Buchmüller, S. Dhamotharan, C. Geweniger, G. Graefe, P. Hanke, G. Hansper, V. Hepp, E.E. Kluge, A. Putzer, J. Sommer, K. Tittel, S. Werner, M. Wunsch

Institut für Hochenergiephysik, Universität Heidelberg, 69120 Heidelberg, Fed. Rep. of Germany¹⁶

R. Beuselinck, D.M. Binnie, W. Cameron, P.J. Dornan,² M. Girone, S. Goodsir, E.B. Martin, N. Marinelli, A. Moutoussi, J. Nash, J.K. Sedgbeer, P. Spagnolo, M.D. Williams

Department of Physics, Imperial College, London SW7 2BZ, United Kingdom¹⁰

V.M. Ghete, P. Girtler, E. Kneringer, D. Kuhn, G. Rudolph

Institut für Experimentalphysik, Universität Innsbruck, 6020 Innsbruck, Austria¹⁸

A.P. Betteridge, C.K. Bowdery, P.G. Buck, P. Colrain, G. Crawford, A.J. Finch, F. Foster, G. Hughes, R.W.L. Jones, M.I. Williams

Department of Physics, University of Lancaster, Lancaster LA1 4YB, United Kingdom¹⁰

I. Giehl, A.M. Greene, C. Hoffmann, K. Jakobs, K. Kleinknecht, G. Quast, B. Renk, E. Rohne, H.-G. Sander, P. van Gemmeren, C. Zeitnitz

Institut für Physik, Universität Mainz, 55099 Mainz, Fed. Rep. of Germany¹⁶

J.J. Aubert, C. Benchouk, A. Bonissent, G. Bujosa, J. Carr,² P. Coyle, F. Etienne, O. Leroy, F. Motsch, P. Payre, M. Talby, A. Sadouki, M. Thulasidas, K. Trabelsi

Centre de Physique des Particules, Faculté des Sciences de Luminy, IN²P³-CNRS, 13288 Marseille, France

M. Aleppo, M. Antonelli, F. Ragusa

Dipartimento di Fisica, Università di Milano e INFN Sezione di Milano, 20133 Milano, Italy

R. Berlich, W. Blum, V. Büscher, H. Dietl, G. Ganis, H. Kroha, G. Lütjens, C. Mannert, W. Männer, H.-G. Moser, S. Schael, R. Settles, H. Seywerd, H. Stenzel, W. Wiedenmann, G. Wolf

Max-Planck-Institut für Physik, Werner-Heisenberg-Institut, 80805 München, Fed. Rep. of Germany¹⁶

J. Boucrot, O. Callot, S. Chen, A. Cordier, M. Davier, L. Duflot, J.-F. Grivaz, Ph. Heusse, A. Höcker, A. Jacholkowska, D.W. Kim,¹² F. Le Diberder, J. Lefrançois, A.-M. Lutz, M.-H. Schune, E. Tournefier, J.-J. Veillet, I. Videau, D. Zerwas

Laboratoire de l'Accélérateur Linéaire, Université de Paris-Sud, IN²P³-CNRS, 91405 Orsay Cedex, France

P. Azzurri, G. Bagliesi,² G. Batignani, S. Bettarini, T. Boccali, C. Bozzi, G. Calderini, M. Carpinelli, M.A. Ciocci, R. Dell'Orso, R. Fantechi, I. Ferrante, L. Foà,¹ F. Forti, A. Giassi, M.A. Giorgi, A. Gregorio, F. Ligabue, A. Lusiani, P.S. Marrocchesi, A. Messineo, F. Palla, G. Rizzo, G. Sanguinetti, A. Sciabà, R. Tenchini, G. Tonelli,¹⁹ C. Vannini, A. Venturi, P.G. Verdini

Dipartimento di Fisica dell'Università, INFN Sezione di Pisa, e Scuola Normale Superiore, 56010 Pisa, Italy

G.A. Blair, L.M. Bryant, J.T. Chambers, M.G. Green, T. Medcalf, P. Perrodo, J.A. Strong, J.H. von Wimmersperg-Toeller

Department of Physics, Royal Holloway & Bedford New College, University of London, Surrey TW20 OEX, United Kingdom¹⁰

D.R. Botterill, R.W. Clift, T.R. Edgecock, S. Haywood, P.R. Norton, J.C. Thompson, A.E. Wright
Particle Physics Dept., Rutherford Appleton Laboratory, Chilton, Didcot, Oxon OX11 0QX, United Kingdom¹⁰

B. Bloch-Devaux, P. Colas, S. Emery, W. Kozanecki, E. Lançon,² M.-C. Lemaire, E. Locci, P. Perez, J. Rander, J.-F. Renardy, A. Roussarie, J.-P. Schuller, J. Schwindling, A. Trabelsi, B. Vallage

CEA, DAPNIA/Service de Physique des Particules, CE-Saclay, 91191 Gif-sur-Yvette Cedex, France¹⁷

S.N. Black, J.H. Dann, R.P. Johnson, H.Y. Kim, N. Konstantinidis, A.M. Litke, M.A. McNeil, G. Taylor

Institute for Particle Physics, University of California at Santa Cruz, Santa Cruz, CA 95064, USA²²

C.N. Booth, C.A.J. Brew, S. Cartwright, F. Combley, M.S. Kelly, M. Lehto, J. Reeve, L.F. Thompson
Department of Physics, University of Sheffield, Sheffield S3 7RH, United Kingdom¹⁰

K. Affholderbach, A. Böhrer, S. Brandt, G. Cowan, C. Grupen, P. Saraiva, L. Smolik, F. Stephan
Fachbereich Physik, Universität Siegen, 57068 Siegen, Fed. Rep. of Germany¹⁶

M. Apollonio, L. Bosisio, R. Della Marina, G. Giannini, B. Gobbo, G. Musolino
Dipartimento di Fisica, Università di Trieste e INFN Sezione di Trieste, 34127 Trieste, Italy

J. Rothberg, S. Wasserbaech
Experimental Elementary Particle Physics, University of Washington, WA 98195 Seattle, U.S.A.

S.R. Armstrong, E. Charles, P. Elmer, D.P.S. Ferguson, Y. Gao, S. González, T.C. Greening, O.J. Hayes, H. Hu, S. Jin, P.A. McNamara III, J.M. Nachtman,²⁴ J. Nielsen, W. Orejudos, Y.B. Pan, Y. Saadi, I.J. Scott, J. Walsh, Sau Lan Wu, X. Wu, G. Zobernig

Department of Physics, University of Wisconsin, Madison, WI 53706, USA¹¹

¹Now at CERN, 1211 Geneva 23, Switzerland.

²Also at CERN, 1211 Geneva 23, Switzerland.

³Also at Dipartimento di Fisica, INFN, Sezione di Catania, Catania, Italy.

⁴Also Istituto di Fisica Generale, Università di Torino, Torino, Italy.

⁵Also Istituto di Cosmo-Geofisica del C.N.R., Torino, Italy.

⁶Supported by the Commission of the European Communities, contract ERBCHBICT941234.

⁷Supported by CICYT, Spain.

⁸Supported by the National Science Foundation of China.

⁹Supported by the Danish Natural Science Research Council.

¹⁰Supported by the UK Particle Physics and Astronomy Research Council.

¹¹Supported by the US Department of Energy, grant DE-FG0295-ER40896.

¹²Permanent address: Kangnung National University, Kangnung, Korea.

¹³Supported by the US Department of Energy, contract DE-FG05-92ER40742.

¹⁴Supported by the US Department of Energy, contract DE-FC05-85ER250000.

¹⁵Permanent address: Universitat de Barcelona, 08208 Barcelona, Spain.

¹⁶Supported by the Bundesministerium für Bildung, Wissenschaft, Forschung und Technologie, Fed. Rep. of Germany.

¹⁷Supported by the Direction des Sciences de la Matière, C.E.A.

¹⁸Supported by Fonds zur Förderung der wissenschaftlichen Forschung, Austria.

¹⁹Also at Istituto di Matematica e Fisica, Università di Sassari, Sassari, Italy.

²⁰Now at Schweizerischer Bankverein, Basel, Switzerland.

²¹Now at University of Geneva, 1211 Geneva 4, Switzerland.

²²Supported by the US Department of Energy, grant DE-FG03-92ER40689.

²³Now at School of Operations Research and Industrial Engineering, Cornell University, Ithaca, NY 14853-3801, U.S.A.

²⁴Now at University of California at Los Angeles (UCLA), Los Angeles, CA 90024, U.S.A.

²⁵Now at Harvard University, Cambridge, MA 02138, U.S.A.

1 Introduction

One approach to the problem of the origin of the masses of the fundamental particles is to postulate the existence of a further layer of structure in nature such that the quarks and leptons, and possibly the gauge bosons, are composite. The fundamental particles at this next level are normally referred to as *preons*, but at present no preon model has been developed which satisfactorily explains the observed spectrum of quarks, leptons and gauge bosons. The most striking evidence of compositeness would be the discovery of excited states of quarks and leptons, or partners of the gauge bosons. Other possible effects are anomalous rates for the decay of the Z boson to three bosons, such as $Z \rightarrow \gamma\gamma\gamma$.

This paper reports an extensive search for such phenomena using data taken with the ALEPH detector during the first phase of LEP running from 1989 to 1995. It is based on approximately 120 pb^{-1} of data taken at the peak of the Z resonance and 40 pb^{-1} off-peak, corresponding to about 4.1 million observed hadronic Z decays. The ALEPH detector and event reconstruction are described in Sections 2 and 3. The largest part of the paper describes direct searches for radiative and weak decays of excited leptons and for excited quarks in Sections 4, 5 and 6 respectively. Section 7 describes searches for a scalar partner of the Z boson and Section 8 describes searches for the “anomalous” decays of the Z boson to $gg\gamma$ and $\gamma\gamma\gamma$. The rest of this introduction discusses the phenomenology of excited fermion production.

All limits given here are at 95% confidence level (c.l.). Systematic uncertainties have been taken into account by adjusting the statistical limit by 1σ of the systematic error. Where appropriate any observed events and the predicted background have been taken into account using the Bayesian approach described in Ref. [1].

Excited fermions could be produced at LEP either singly or in pairs, as shown in Fig. 1. Sequential type particles are commonly assumed when searching for pair production. At LEP 1, pair production is dominated by s -channel Z exchange (Fig. 1(a)), with (b) and (c) suppressed by the magnetic couplings at the Ze^*e , γe^*e and $W\nu_e^*e$ vertices (see below). The total cross-section and the angular distribution are then given by the Standard Model provided the anomalous magnetic moments of the excited fermions are zero. In this particular case there is no dependence on the compositeness energy scale, and lack of observation of a signal allows a limit to be set on the f^* mass. If the cross-section is suppressed by effective form factors then limits can be set on these as a function of f^* mass.

Single production and decay occurs through a magnetic type coupling to gauge bosons (Fig. 1(a) – (c)). At LEP 1, s -channel Z exchange and t -channel photon exchange should dominate. A convenient general parametrization for the contribution to the Lagrangian from s -channel Z exchange is [1]

$$\mathcal{L} = \frac{\lambda_Z e}{2m_{f^*}} \bar{f}^* \sigma^{\mu\nu} \left(\eta_L \frac{1 - \gamma_5}{2} + \eta_R \frac{1 + \gamma_5}{2} \right) f Z_{\mu\nu} + \text{h.c.} \quad (1)$$

Similar terms exist for W and γ exchange.

A $U(1) \times SU(2)$ invariant model for the single production and decay of excited leptons, ℓ^* , containing both left- and right-handed particles (homodoublet model) has been developed by several authors [2–4] with the general form of Lagrangian

$$\mathcal{L} = \frac{1}{2\Lambda} \bar{L}^* \sigma^{\mu\nu} \left(gf \frac{\tau}{2} W_{\mu\nu} + g' f' Y B_{\mu\nu} \right) \frac{1 - \gamma_5}{2} L + \text{h.c.} \quad (2)$$

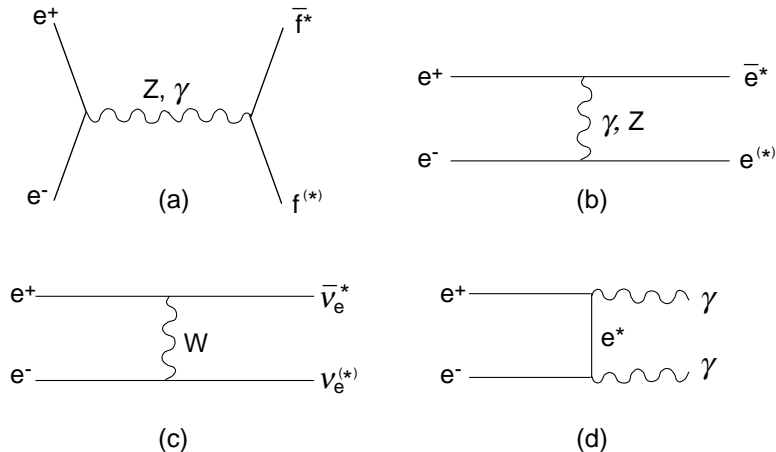


Figure 1: (a) – (c) Single and double production processes for excited fermions. (a) s -channel Z and γ exchange, (b) t -channel Z and γ exchange, (c) t -channel W exchange. (d) t -channel e^* exchange producing two photons. The symbol $f^{(*)}$ implies a fermion or its excited partner as appropriate.

where L is the lepton doublet, g and g' are the Standard Model gauge couplings, f and f' are the corresponding couplings for the magnetic transition, τ are the Pauli spin matrices and Y is the weak hypercharge; Λ is the compositeness energy scale. When more than one process can contribute to ℓ^* production, for example s -channel γ and Z exchange at LEP 2, it is normal to assume some relationship between f and f' and to give limits in terms of λ/m_{ℓ^*} , defined as $f/\sqrt{2}\Lambda$. However when one exchange process dominates, as at LEP 1, an alternative form of the Lagrangian is convenient [3]

$$\mathcal{L} = \frac{e}{2\Lambda} \bar{L}^* \sigma^{\mu\nu} (c_{Z\ell^*\ell} - d_{Z\ell^*\ell} \gamma_5) LZ_{\mu\nu} + \text{h.c.} \quad (3)$$

where $c_{Z\ell^*\ell}$ and $d_{Z\ell^*\ell}$ are linear combinations of f and f' , and also depend on the weak mixing angle θ_W ; assuming CP conservation then $c_{Z\ell^*\ell} = d_{Z\ell^*\ell}$. Now no assumptions are needed about f and f' and equations (1) and (3) are related by $\lambda_Z/m_{\ell^*} = 2c_{Z\ell^*\ell}/\Lambda$. Similar expressions hold for couplings to the other gauge bosons. In the literature limits have been presented in terms of both of these parameters; in this paper they are given for $Z\ell^*\ell$ and γe^*e couplings in terms of c/Λ .

Limits for excited quark production are normally given in terms of λ/m_{q^*} and that convention is followed in section 6.

2 The ALEPH detector

The construction of the ALEPH detector [5] and its performance [6] have been described previously; only a brief summary is given here.

Charged particles are bent in the 1.5 T axial magnetic field produced by a superconducting solenoid and are tracked in the silicon vertex detector (VDET), the inner tracking chamber (ITC) and the time projection chamber (TPC). The momentum

resolution for a track reaching the outer radius of the TPC is $\Delta p/p = 0.0006p_t \oplus 0.005$ for transverse momentum, p_t , in GeV/ c . The track finding efficiency is good down to an angle of about 15° from the beam direction and track cuts are normally made at $|\cos\theta| < 0.95$ (18°). Track momentum is well-measured down to about 200 MeV/ c and, in the searches described here, a momentum cut of 500 MeV/ c has been applied.

The electromagnetic calorimeter (ECAL) consists of 45 layers of lead and proportional wire chamber planes with 22 radiation lengths of material. It is subdivided into a barrel and two endcaps each containing twelve modules. The longitudinal structure is the same in all modules. The total signal from each anode plane of each module is read out, providing a detailed profile in depth of the energy deposition. The cathode planes of each layer are subdivided into pads approximately 30×30 mm² which are connected internally to form projective towers. Each tower is read out in three sections in depth (“storeys”) containing 4, 9 and 9 radiation lengths respectively. The storeys form the basis of the identification of showers in the calorimeter through the definition of a “cluster”, which is the collection of all storeys with an energy above a threshold of 30 MeV which have at least a corner in common. The highly granular structure of ECAL (about $0.9^\circ \times 0.9^\circ$) provides excellent identification of electrons, photons and neutral pions, even in dense hadronic jets. The energy and angular resolutions are respectively

$$\frac{\sigma_E}{E} = \frac{0.18}{\sqrt{E(\text{GeV})}} + 0.009 \quad \text{and} \quad \sigma_{\theta,\phi} = \frac{2.5}{\sqrt{E(\text{GeV})}} + 0.25 \text{ mrad}.$$

The endcap sensitive region extends down to 13° from the beam axis. Much of the remaining solid angle (between 11° and 2.6°) is covered by the luminosity calorimeter (LCAL), with similar structure to ECAL. From September 1992 a silicon calorimeter (SiCAL) was added to provide a more precise luminosity measurement and covers the region down to 1.4° . The ability to detect electromagnetic energy deposits in regions close to the beam axis is important in many searches.

The hadron calorimeter consists of 23 layers of plastic streamer tubes separated by 50 mm iron slabs (7.2 interaction lengths in total). There are twelve modules in the barrel section and six in each endcap. HCAL and ECAL are rotated relative to each other by about 2° to avoid alignment of cracks. Thus an electron passing through a crack in ECAL is detected in HCAL, albeit with a worse energy resolution. The sensitive region in the endcap of HCAL extends down to 8° from the beam direction so that the small gap between ECAL and LCAL is also covered. Signals are induced on electrodes on both sides of the streamer tubes. The open side of the cells faces copper cathode pads which, as in ECAL, are constructed to form projective towers. The granularity is such that one tower in HCAL matches approximately 4×4 towers in ECAL. The signals from all pads in a tower are summed. On the other side of the tubes aluminium strips run along the length of each tube to give a signal whenever that particular tube fires. The readout of this digital (binary) signal provides a two-dimensional picture of showers in the calorimeter which plays a crucial role in particle identification. The relative energy resolution of HCAL is approximately $80\%/\sqrt{E}$. Two double layers of the same streamer tubes (“muon chambers”) surround the detector and improve muon identification. These chambers have orthogonal readout strips thus providing a space point in each one.

3 General analysis procedures

Unless otherwise stated the analyses described in this paper have used standard ALEPH algorithms for particle identification [7] which are now briefly described.

Identification of electron and photon showers is based on two estimators which are constructed to have zero mean and unit variance for electrons. The first, R_T , measures the ratio E_4/p , where E_4 is the energy deposited in the four towers closest to an extrapolated track and p is the track momentum. The second, R_L , is based on the mean position of the longitudinal energy deposit of the shower and measures the degree to which the observed longitudinal profile matches that expected for an electron. An additional estimator, R_I , is based on the track ionization measurement, dE/dx , made in the TPC. It provides an independent identification procedure that is particularly effective at low momentum and is hence complementary to R_T and R_L . Photon conversions in the tracking detectors are recognised by the opening angle and reconstructed invariant mass of the two tracks.

Muons are identified by extrapolating tracks through HCAL and to the muon chambers. Identification criteria are based on the mean number of hits per plane and the total number of planes fired in HCAL, and on muon chambers hits.

The total energy flow [6] in an event or part of an event is an important feature of many searches. The high granularity of the ALEPH calorimeters greatly aids the calculation of this quantity *via* the matching of tracks and calorimeter energy deposits. It is calculated from as complete a list as possible of all particles in the event, made as follows. The measured momenta of all charged tracks are used to identify their associated energy deposits in the calorimeters, which are then discounted in calculating the neutral energy. Photons are identified in the electromagnetic calorimeter and π^0 s found from these. Remaining calorimeter deposits are identified as neutral hadrons with an appropriate correction for the different response of ECAL to electrons and pions. Clusters found in LCAL are included. The energy flow is then calculated from the energy of all particles found. It has a resolution for hadronic events of 6.2 GeV.

Jet finding has been carried out using the JADE algorithm [8, 9]. The value of the parameter y_{cut} used in the algorithm has been tuned separately for the different searches.

In the analysis of events, parameters such as mass resolution can be greatly improved by applying energy and momentum conservation. Because of ALEPH's excellent angular resolution for both charged tracks and photons this is most readily achieved by rescaling energy measurements without changing measured angles. This procedure has been applied to events in many of the channels described in this paper.

Veto inefficiencies due to beam-related backgrounds have been monitored using randomly triggered events. They are small in all cases—typically less than 0.5%.

4 Search for radiative decays of excited leptons

In this section searches for excited charged leptons and neutrinos followed by radiative decay are described. The signal for charged leptons is a peak in the $\ell\gamma$ invariant mass plot, on top of the background from radiative lepton pair production. Searches for excited neutrinos have been made by counting events within the kinematically allowed photon energy range for a given mass. A search for virtual e^* effects on the angular distribution for the reaction $e^+e^- \rightarrow \gamma\gamma$ (Fig. 1(d)) has also been made.

4.1 Excited charged leptons

4.1.1 The process $e^+e^- \rightarrow (e^\pm)e^\mp\gamma$

A search has been made for resonant e^* production in the process $e^+e^- \rightarrow (e^\pm)e^{*\mp} \rightarrow (e^\pm)e^\mp\gamma$, in which a photon emitted by one beam particle scatters from one of opposite charge in the other beam. Such events have an energetic charged track and photon in the detector, coplanar with the beam, the other particle remaining in the beampipe. The sum of the energies of the two observed particles is larger than the beam energy and the event is boosted in the direction of the beam of the same sign as the charged track.

An irreducible background to e^* production arises from radiative Bhabha scattering, with one of the particles escaping down the beampipe, known as the quasi-real Compton process [10] (background (i)). Other backgrounds are (ii) large angle Bhabha scattering when one of the final state electrons transfers almost all of its energy to a photon through bremsstrahlung in the detector material before the TPC, and (iii) $\gamma\gamma$ final states where one of the photons converts into an e^+e^- pair and one member of the pair escapes detection. These three backgrounds were simulated using the Monte Carlo generators TEEGG7 [11], BHWIDE [12] and GGG [13].

Two initial cuts were applied in the search: the charged track and photon energies were each required to be greater than 10 GeV, and the photon was required to be coplanar within $\pm 1^\circ$ with the observed electron and the beam. Then, assuming a three-particle final state and using only the measured angles of the charged track and the photon, the energy, E_{miss} , of the missing beam particle was determined. Events with further missing energy due to additional photons at low polar angle were then rejected by requiring that the sum of E_{miss} and the measured energies of the observed particles had to be greater than $0.9\sqrt{s}$. At this stage 26432 events remained while 24337 are expected. However there is a large number of events arising from backgrounds (ii) and (iii) in which the photon and the charged track have an opening angle larger than 175° . Since each charged track normally produces 8 hits in the ITC, background (ii) was removed by requiring fewer than 12 ITC hits in total in such events, and background (iii) was removed by requiring at least 4 ITC hits. Following this cut 7789 events survive while 7305 are expected.

In the e^* centre of mass frame, the decay photon is preferentially scattered forward [3], whereas the quasi-real Compton process favours backscattered photons [10]. This effect was exploited to enhance signal sensitivity by imposing a cut on θ_γ , the photon scattering angle in the laboratory frame, which varies linearly with e^* mass, with θ_γ required to be less than 160° at $18 \text{ GeV}/c^2$ and less than 120° at $90 \text{ GeV}/c^2$. To further reject events arising mainly from background (ii), θ_γ was also required to be greater than 30° , independent of mass.

Finally the charged particle was required to pass the standard ALEPH electron identification criteria, and the sign of its charge had to be that of the beam particle interacting with the quasi-real photon. The final sample contains 4045 events, in good agreement with the 3960 predicted, comprising 3809, 142 and 9 events from backgrounds (i) to (iii) respectively.

The $e\gamma$ invariant mass is most precisely determined using the measured angles of the charged particle and the photon and the centre of mass energy. It is shown in Fig. 2(a) for the final sample of events. The mass resolution is $0.075 \text{ GeV}/c^2$, almost independent of mass. There is no evidence for a peak due to e^* production and the shape of the distribution agrees well with the Monte Carlo prediction (not shown).

4.1.2 The processes $e^+e^- \rightarrow \ell^+\ell^-\gamma$ and $e^+e^- \rightarrow \ell^+\ell^-\gamma\gamma$

The search for ℓ^* in these channels was made using events with two, four or six charged tracks and one or more photons. In events with more than two tracks, searches were first made for tau decays, defined as three tracks with an invariant mass less than m_τ and a total charge of ± 1 , with neutral clusters added if the resultant invariant mass was less than $2 \text{ GeV}/c^2$. Events were then selected if they contained one or two photons with energy above 10 GeV and isolated by at least 25° from a charged particle (or reconstructed tau). For the two-prong topology the acollinearity of the two tracks was required to be between 5° and 175° .

The selection of the $e^+e^-(n\gamma)$ final state was made by requiring the ECAL energy due to the charged tracks to be greater than $0.7(\sqrt{s} - E_\gamma)$, where E_γ is the sum of the energies of isolated photons. At least one track was required to pass the standard ALEPH electron identification criteria, removing 80 events which are principally tau pairs. The final sample consists of 4234 $e^+e^-\gamma$ events compared to 4333 predicted by BHWIDE plus 19 remaining tau pairs. Eighteen $e^+e^-\gamma\gamma$ events, potential $e^*\bar{e}^*$ candidates, were found.

To select $\mu^+\mu^-(n\gamma)$ events the ECAL energy deposited by the two charged tracks was required to be less than $0.1(\sqrt{s} - E_\gamma)$. This cut removed all the Bhabha events and a large fraction of the $\tau^+\tau^-$ events. Requiring the sum of the charged particle momenta and photon energy to be greater than $0.8\sqrt{s}$ removed further τ background. Finally at least one track was required to satisfy the standard ALEPH muon identification requirements, removing 80 events. The final $\mu^+\mu^-\gamma$ sample consists of 2738 events, compared to 2788 predicted for this channel by KORALZ [14] and 44 from $\tau^+\tau^-$. Twenty $\mu^+\mu^-\gamma\gamma$ events, potential $\mu^*\bar{\mu}^*$ candidates, were found.

The $\tau^+\tau^-(n\gamma)$ selection was made on two-, four- and six-prong events after reconstruction of τ s as described above. In the two-prong topology the missing mass squared was required to be greater than $600 (\text{GeV}/c^2)^2$ and in the four- and six-prong topologies it was required to be greater than $300 (\text{GeV}/c^2)^2$. Background from $\mu^+\mu^-\gamma$ was removed by requiring the sum of the charged particle momenta to be less than $0.9(\sqrt{s} - E_\gamma)$. The final $\tau^+\tau^-\gamma$ sample consists of 2216 events compared to 2134 predicted by KORALZ, together with 64 e^+e^- and 2 $\mu^+\mu^-$ events. Twenty-four $\tau^+\tau^-\gamma\gamma$ events, potential $\tau^*\bar{\tau}^*$ candidates, were found.

The number of pair production candidates in each channel is not correctly predicted by the background Monte Carlo generators, which have missing higher orders. However they agree well with the second order matrix element calculation of Ref. [15].

The invariant ℓ^* candidate masses for the final states $e^+e^-\gamma$ and $\mu^+\mu^-\gamma$ were calculated by rescaling the particle energies to conserve energy and momentum (including the effect of an initial state photon in the beampipe) using the measured angles. The resulting invariant mass resolution is about $0.075 \text{ GeV}/c^2$ and is approximately independent of mass. In the $\tau\gamma$ channel there are unobserved neutrinos. However, the τ momenta can be calculated by assuming that the original τ directions are the same as those of the visible decay products and rescaling their momenta by imposing energy and momentum conservation. The resulting invariant mass resolution is around $1.5 \text{ GeV}/c^2$ independent of τ^* mass. No initial state photon was included in the calculation in this case since it degrades the mass resolution. The invariant mass distributions are shown in Fig. 2(b)–(d). The shapes are well described by Monte Carlo.

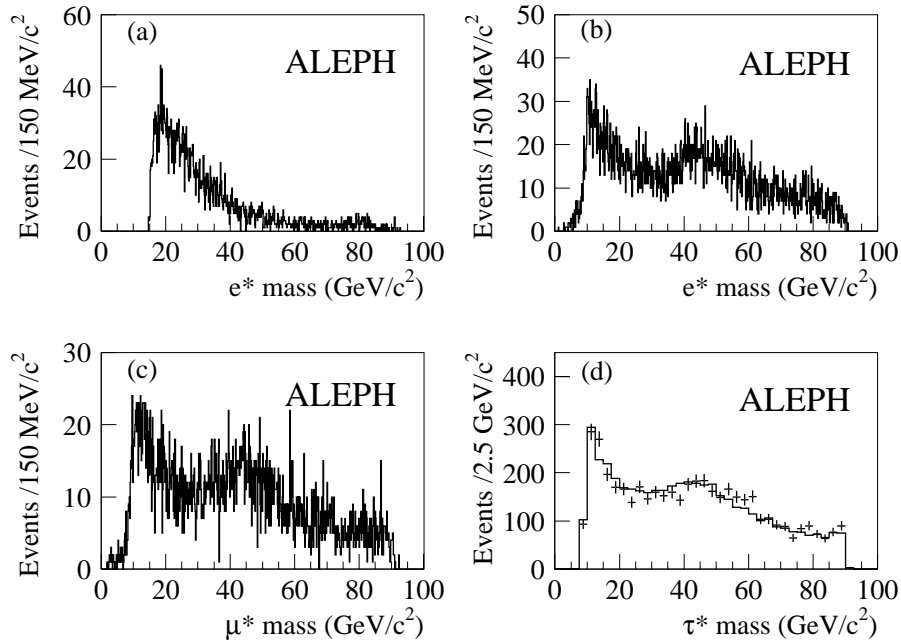


Figure 2: $\ell\gamma$ invariant mass distributions for the final states (a) $e\gamma$, (b) $e^+e^-\gamma$, (c) $\mu^+\mu^-\gamma$ and (d) $\tau^+\tau^-\gamma$. There are two entries per event except in (a). In (d) the Standard Model background prediction is shown by the solid histogram and the data by crosses. The bin widths have been chosen to be about twice the resolution.

4.1.3 Form factor limits from the $\ell^*\bar{\ell}^*$ channels

The detection efficiency for $\ell^*\bar{\ell}^*$ production and the ℓ^* invariant mass resolutions were determined using a modified version of the KORALZ generator. There are two ℓ^* combinations per event and the one with the smaller ℓ^* invariant mass difference was selected. The resolution on the mass difference is $0.35\text{ GeV}/c^2$ for e^*e^* and $\mu^*\bar{\mu}^*$, and $2.5\text{ GeV}/c^2$ for $\tau^*\bar{\tau}^*$. After requiring the mass difference to be less than 2σ of the resolution one $\mu^+\mu^-\gamma\gamma$ event and three $\tau^+\tau^-\gamma\gamma$ events survived. Over most of the mass range the efficiencies are approximately 50% for the e^*e^* and $\mu^*\bar{\mu}^*$ channels, and 30% for $\tau^*\bar{\tau}^*$.

Assuming Standard Model couplings and the calculated detection efficiency, the expected number of events is predicted as a function of mass. Mass limits of $46\text{ GeV}/c^2$ have already been set by ALEPH at LEP 1 [16] and these have recently been superseded by higher energy data [17]. The present search is used to set a limit on the factor by which the coupling must be multiplied (effectively a form factor for compositeness) as a function of ℓ^* mass (Fig. 3). For masses between 10 and $40\text{ GeV}/c^2$ this limit is of the order of 1%. Below about $5\text{ GeV}/c^2$, where the efficiency for the direct search is very small, limits derived from Z partial width limits (Appendix A) are better.

4.1.4 Coupling limits from the $\ell^*\ell$ channels

The cross-section for single production has been calculated using the formalism of Ref. [3], with $f = f'$ in equation (2). The detection efficiency was determined using the generator of Ref. [18] for the e^*e and quasi-real Compton scattering channels, and that of Ref. [19] for $\mu^*\mu$ and $\tau^*\tau$. Events were generated at discrete ℓ^* masses over the full range and passed

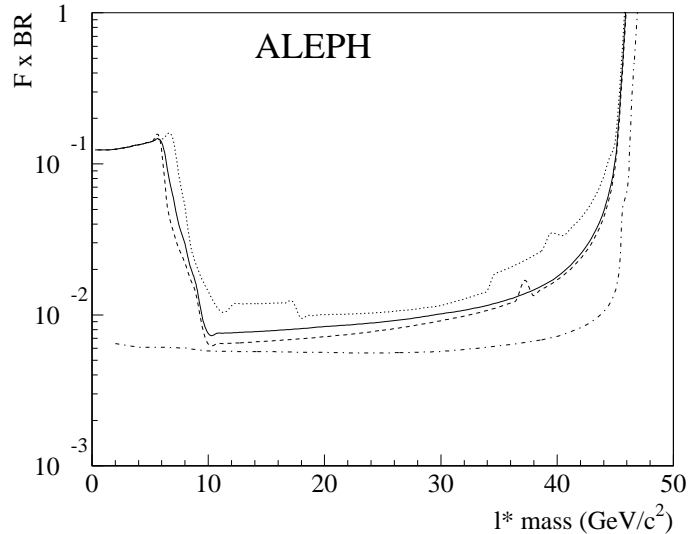


Figure 3: Form factor times branching ratio limits at 95% c.l. for fermion pair production followed by radiative decay. The solid, dashed, dotted and dot-dashed curves are for e^*e^* , $\mu^*\bar{\mu}^*$, $\tau^*\bar{\tau}^*$ and a single flavour $\nu^*\bar{\nu}^*$ respectively. Below about $5 \text{ GeV}/c^2$ the limits have been derived from Z partial width limits. Values above the curves are excluded.

through the ALEPH simulation and reconstruction program chain. The efficiency for e^* in the quasi-real Compton scattering channel increases linearly from zero at $14 \text{ GeV}/c^2$ to about 70% at $91 \text{ GeV}/c^2$. For e^* s -channel production and μ^* , the efficiencies are around 60% and 65% respectively, independent of mass; for τ^* it is about 52%.

The branching ratio for photonic decay has been calculated according to Ref. [4]; it is expected to be close to 100% for $m_{\ell^*} < m_W$, but to decrease to 85% at $90 \text{ GeV}/c^2$. Coupling limits have been calculated as a function of mass in bins of width 4σ , where σ is the appropriate mass resolution and are shown in Fig. 4. The s -channel process dominates the $\ell^+\ell^-\gamma$ final state and the limit derived is on the coupling $c_{Z\ell^*\ell}$. The limit for the t -channel process $e^+e^- \rightarrow (e^\pm)e^*\bar{e} \rightarrow (e^\pm)e^*\bar{e}\gamma$, dominated by photon exchange, is on the coupling $c_{\gamma e^*e}$.

4.1.5 An e^* limit from $e^+e^- \rightarrow \gamma\gamma$

Electron-positron annihilation into two photons occurs by t -channel electron exchange, and so is described by Quantum Electrodynamics with negligible electroweak corrections. The exchange of a virtual e^* can also contribute and the modified cross-section then depends on both the excited electron mass, m_{e^*} , and the ratio of the $e^*e\gamma$ to $ee\gamma$ couplings.

Events containing two or more photons and no additional particles were selected. After being transformed into the centre-of-mass frame of the two most energetic photons (to remove the effects of initial state radiation), the number of events as a function of the cms scattering angle was compared with that predicted by QED. A log-likelihood fit was performed on the observed angular distribution to determine the 95% c.l. upper limit on $c_{\gamma e^*e}/\Lambda$ as a function of m_{e^*} (Fig. 5). Also shown on the figure is the value of $1/(2m_{e^*})$, showing that the 95% c.l. lower limit on the mass of the excited electron is $160 \text{ GeV}/c^2$ if the γe^*e coupling is the same as that for γee , i.e. $\lambda_{\gamma e^*e} = 1$.

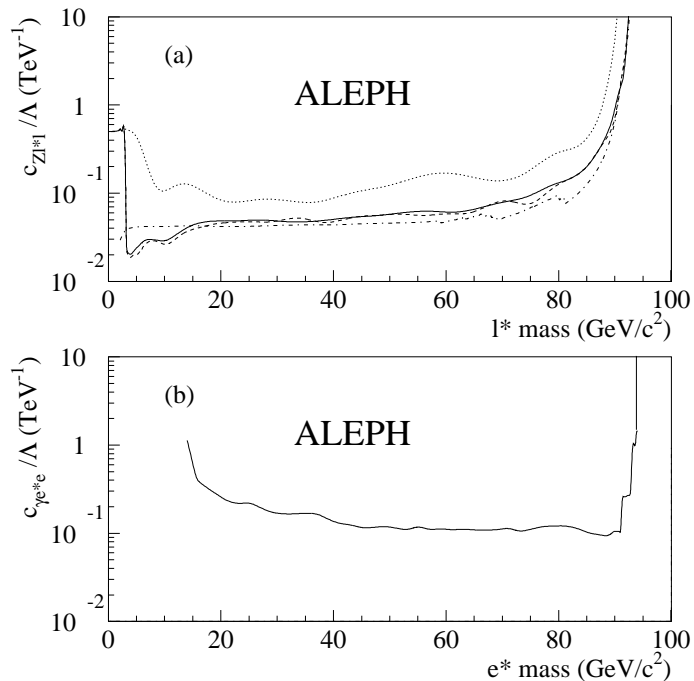


Figure 4: Coupling limits for single excited lepton production derived from the search for radiative decays and assuming decay branching ratios as described in the text. (a) s -channel: solid, dashed, dotted and dot-dashed curves denote e^* , μ^* , τ^* and ν^* respectively; (b) t -channel e^* . In (a) the limits below $5 \text{ GeV}/c^2$ have been derived from Z width limits. Values above the curves are excluded at 95% c.l.

4.2 Excited neutrinos

The excited neutrino, ν^* , is expected to be the lightest excited particle [4] and it may have either radiative or weak decays. If in equation (2) $f = f'$, then the decay $\nu^* \rightarrow \nu\gamma$ is forbidden. However there is no particular reason for this assumption and it is therefore also important to search for this decay mode.

Pair-production of ν^* should have a cross-section given by the Standard Model, possibly modified by form factors. The experimental signature is two acoplanar photons. Monte Carlo signal events were again produced using the modified KORALZ generator. The backgrounds considered were second order initial state radiation (ISR) accompanying neutrino pair production ($\nu\bar{\nu}\gamma\gamma$), also simulated with KORALZ, and the $\gamma\gamma$ final state, including first order ISR, simulated by GGG. The potential background from Bhabha events with two radiated photons was eliminated by a cut of 8° on the predicted angle of the deflected beam particle, with negligible effect on the signal efficiency. The effectiveness of this cut was confirmed using BHABMC [20]. Events were selected with two photonic clusters above 3 GeV in the electromagnetic calorimeter, with a veto on charged tracks, additional electromagnetic clusters above 0.5 GeV , hadronic clusters above 2 GeV , or more than 0.5 GeV of energy below a polar angle of 12° . There are 3425 data events remaining at this stage, with 3483 predicted by the GGG Monte Carlo and 1.5 by the radiative neutrino Monte Carlo.

Multiphoton QED events are coplanar, and a cut was made at 160° on the angle between the two clusters projected onto the plane perpendicular to the beam. Low mass

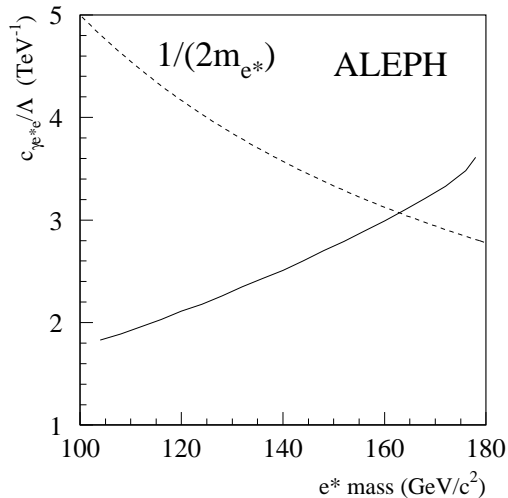


Figure 5: 95% c.l. upper limit on $c_{\gamma e^*}/\Lambda$ (solid curve) as a function of m_{e^*} . Also plotted (dotted curve) is $1/2m_{e^*}$; the intersection of the two curves gives the lower limit for the mass of the e^* if the γe^*e coupling is the same as γee . This figure extends the limit shown on Fig. 4(b) to higher mass.

ν^* signal events fail this cut due to the relativistic collimation of the decay products. Therefore events were also accepted if one of the two photons had less than 70% of beam energy and the event could not be reconstructed as a three photon event with one photon in the beampipe. The predicted background is 1.8 events from $\gamma\gamma(\gamma)$ and 1.5 from $\nu\bar{\nu}\gamma\gamma$, and 2 events are seen in data. Signal efficiencies rise uniformly from 29% for a ν^* mass of $2\text{ GeV}/c^2$ to 57% at $45\text{ GeV}/c^2$. Fig. 3 shows the 95% c.l. form factor limit for $\nu^*\bar{\nu}^*$ production assuming 100% radiative decay.

For the single production channel, the signature is one photon in an otherwise empty event. The photon energy spectrum is uniformly distributed in the interval from $m_{\nu^*}^2/2\sqrt{s}$ to $\sqrt{s}/2$. The backgrounds studied were radiative Bhabha events, where the beam particles remain in the beampipe, radiative neutrino pair production and QED multiphoton final states. The same test on the predicted angle of the deflected beam particle as above eliminated all Monte Carlo Bhabha events (using ten times more events than in the data). A large fraction of the radiative neutrino background is also removed by this cut. The remaining background events are at low polar angle or have low total energy.

Requiring the photon energy to be above 18 GeV, there are 33 events in data, with 21.5 predicted by GGG and 14.4 by the neutrino pair Monte Carlo. Using only the calorimeter barrel region ($45^\circ < \theta_\gamma < 135^\circ$) optimizes the sensitivity of the search. In this region there are 7 events in the data compared with 7.6 events predicted by the radiative neutrino Monte Carlo and 0.3 by GGG. No mass determination is possible and the limit at each mass value was determined from the number of data and Monte Carlo events with a photon in the kinematically allowed energy range. Coupling limits calculated for $f = 1$, $f' = 0$ in equation (2), with the photonic branching ratio calculated as in Ref. [4], are shown in Fig. 4. The branching ratio is close to 100% for $m_{\nu^*} < m_W$, but decreases to 85% at $90\text{ GeV}/c^2$.

4.3 Summary

No evidence has been found for single or double excited lepton production in radiative events. For double production, form factor times branching ratio limits have been set which are of order 0.01 for masses between 10 and 40 GeV/c². Limits on the couplings c/Λ for single production are below 0.1 TeV⁻¹ for masses up to about 80 GeV/c². Virtual e^* exchange with Standard Model coupling has been excluded for masses up to 160 GeV/c² in the reaction $e^+e^- \rightarrow \gamma\gamma$. These searches, using the whole LEP I data sample, update those previously published by ALEPH [16].

Limits on these channels have also been published by the other LEP collaborations at LEP 1 [21–25] and from higher energy running [17, 26–32]. Experiments at HERA [33, 34] have set e^* coupling limits which are somewhat worse than those reported here for $m_{e^*} \sim 50$ GeV/c² but which extend up to 250 GeV/c².

5 Search for weak decays of excited leptons

If in equation (2) $f = f'$ radiative decays of excited charged leptons dominate for $m_{\ell^*} < m_W$. However, for other assumptions weak decays of both ℓ^* and ν^* are expected to contribute significantly [35]. Thus, with no assumptions about f and f' , a systematic search of the ALEPH data has been carried out for single and pair production of excited leptons followed by their decay *via* virtual W or Z. Both leptonic and hadronic final states can be produced and the searches for these are described separately in Sections 5.1 and 5.2 before the limits derived are combined.

For double ℓ^* production, the mass range is limited to $\sqrt{s}/2$ and the total cross-section and angular distribution are given by the Standard Model. There is no dependence on the compositeness scale Λ , although a form factor can be applied. For single production the formalism of Ref. [3], described in Section 1, has been used.

The weak decay of an excited lepton is a three-body decay process involving the emission of virtual W or Z bosons which in turn decay into a fermion-antifermion pair (Fig. 6). The dynamics of this decay has been fully described in Ref. [4]. In this analysis the excited lepton mass has been limited to below m_W in charged current (CC) decays and to below m_Z in neutral current (NC) decays. In calculating the branching ratios of the virtual W and Z bosons, the effect of the b quark mass has been taken into account.

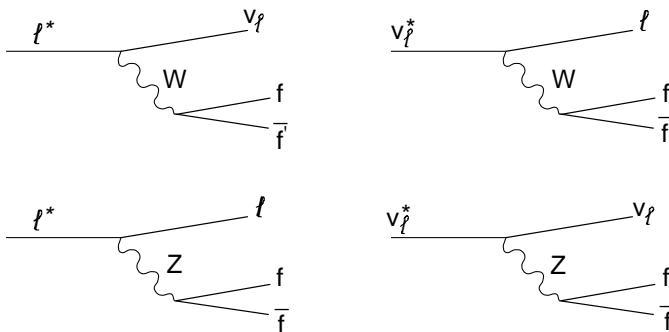


Figure 6: Weak decays of excited leptons.

Hadronization of the $q\bar{q}$ pair is carried out in the LUND framework [36] with parton showers followed by string fragmentation. Quark masses and flavours, and the $q\bar{q}$ invariant mass, $\sqrt{Q^2}$, are taken into account. The value of Q^2 constrains the proportions of $q_i\bar{q}_j$ pairs through the hadronic widths of the off-shell W and Z bosons (whose analytic forms are given in Ref. [37]).

5.1 Search for leptonic final states

The event topology arising from weak decay of excited leptons depends on the production and decay chain as summarized in Table 1. Different searches were therefore carried out for two-, four- and six-prong events.

Table 1: Possible leptonic final states in weak decays of excited leptons.

Channel	Weak decay	Final state topology	Charged multiplicity	Missing energy?
$\ell^*\ell$	$\ell\ell Z$	$\ell^+\ell^-\ell^+\ell^-$	4	No
$\ell^*\ell$	$\ell\ell Z$	$\ell^+\ell^-\nu\bar{\nu}$	2	Yes
$\ell^*\ell$	$\ell\nu W$	$\ell^+\ell^-\nu\bar{\nu}$	2	Yes
$\nu^*\nu$	$\nu\nu Z$	$\ell^+\ell^-\nu\bar{\nu}$	2	Yes
$\nu^*\nu$	$\ell\nu W$	$\ell^+\ell^-\nu\bar{\nu}$	2	Yes
$\ell^*\bar{\ell}^*$	$\ell\ell ZZ$	$\ell^+\ell^-\ell^+\ell^-\ell^+\ell^-$	6	No
$\ell^*\bar{\ell}^*$	$\ell\ell ZZ$	$\ell^+\ell^-\ell^+\ell^-\nu\bar{\nu}$	4	Yes
$\ell^*\bar{\ell}^*$	$\ell\ell ZZ$	$\ell^+\ell^-\nu\bar{\nu}\nu\bar{\nu}$	2	Yes
$\ell^*\bar{\ell}^*$	$\ell\nu ZW$	$\ell^+\ell^-\ell^+\ell^-\nu\bar{\nu}$	4	Yes
$\ell^*\bar{\ell}^*$	$\ell\nu ZW$	$\ell^+\ell^-\nu\bar{\nu}\nu\bar{\nu}$	2	Yes
$\ell^*\bar{\ell}^*$	$\nu\nu WW$	$\ell^+\ell^-\nu\bar{\nu}\nu\bar{\nu}$	2	Yes
$\nu^*\bar{\nu}^*$	$\nu\nu ZZ$	$\ell^+\ell^-\ell^+\ell^-\nu\bar{\nu}$	4	Yes
$\nu^*\bar{\nu}^*$	$\nu\nu ZZ$	$\ell^+\ell^-\nu\bar{\nu}\nu\bar{\nu}$	2	Yes
$\nu^*\bar{\nu}^*$	$\ell\nu ZW$	$\ell^+\ell^-\ell^+\ell^-\nu\bar{\nu}$	4	Yes
$\nu^*\bar{\nu}^*$	$\ell\nu ZW$	$\ell^+\ell^-\nu\bar{\nu}\nu\bar{\nu}$	2	Yes
$\nu^*\bar{\nu}^*$	$\ell\ell WW$	$\ell^+\ell^-\ell^+\ell^-\nu\bar{\nu}$	4	Yes

5.1.1 Events with two acollinear charged tracks

The main backgrounds come from the processes $e^+e^- \rightarrow \ell^+\ell^-(\gamma)$, $e^+e^- \rightarrow e^+e^-\ell^+\ell^-(\gamma)$ and $e^+e^- \rightarrow e^+e^- + \text{hadrons}$. A large number of these background events were rejected by simple kinematic requirements, namely exactly two well-reconstructed tracks with opposite charges and momenta larger than 1 GeV/c, missing transverse momentum greater than 8 GeV/c, and scalar sum of track momenta between 6 and 82 GeV/c. The lower cut and the missing transverse momentum cut act against two-photon events while the upper one rejects e^+e^- annihilations into leptons. Events with isolated neutral clusters above 100 MeV were also removed.

No single set of cuts removes the remaining background (dominated by $\tau^+\tau^-(\gamma)$) while maintaining a high signal efficiency for all channels because of the kinematic and

topological differences between them. Thus for e^* and μ^* single production, two kinematic configurations have been defined according to the ℓ^* mass — low ($\leq 30 \text{ GeV}/c^2$) and high ($> 30 \text{ GeV}/c^2$). At low mass these channels are distinguished by an energetic lepton, thus at least one track with a momentum greater than $36 \text{ GeV}/c$ was required. To reject the remaining background ($e^+e^-\gamma$ and $\tau^+\tau^-$) the acollinearity angle was required to be less than 165° . For the high mass configuration, the distribution of the signal acollinearity angle allows a more severe cut to be made at 155° . For the reactions $\nu^*\nu$, $\tau^*\tau$, $\ell^*\bar{\ell}^*$ and $\nu^*\bar{\nu}^*$, the acollinearity and acoplanarity angles were required to be smaller than 165° and 170° respectively.

After these cuts there is good agreement between the number of observed events and expected backgrounds (Table 2). The main source of background is still $\tau^+\tau^-$ events.

Table 2: Number of observed and expected events in the two-prong search.

Reaction	Set of cuts	Candidates	Expected
$e^+e^- \rightarrow \ell^*\ell$	low masses	1	2.2
$e^+e^- \rightarrow \ell^*\ell$	high masses	8	6.9
$e^+e^- \rightarrow \nu^*\nu, \ell^*\bar{\ell}^*, \nu^*\bar{\nu}^*$	all masses	9	12.2

The efficiency depends on the ℓ^* flavour and mass and its decay mode (CC or NC). The efficiency varies from 40% to 70% for $\mu^*\mu$ and from 20% to 55% for e^*e . For ν^* pair production, it is between 40% and 50% over the whole mass range, while for ℓ^* pair production it increases with mass from 20% to 50%.

In the case of $\tau^*\tau$, the analysis described above has a very low efficiency (close to 5%), due mainly to the veto on neutral clusters. However a multi-variable analysis based on a multi-layer neural network has been performed in this channel which has a much higher efficiency [38]. It consists of an input layer of nine neurons corresponding to the principal kinematic variables of the signal, and two intermediate layers with five and three neurons respectively. The learning phase required a sample of 800 $\tau^*\tau$ signal events and another of 800 background events. The final response is insensitive to the τ^* mass and in the mass range $10 \text{ GeV}/c^2$ to $80 \text{ GeV}/c^2$ the signal efficiency is 25%. No data events remain after the neural network analysis while the expected background is compatible with zero.

5.1.2 Search for four-prong final states

Events with four well-reconstructed tracks and zero total charge were selected, rejecting those with photon conversions or energy deposition in LCAL. Two-photon events were rejected by requiring a scalar sum of track momenta greater than $16 \text{ GeV}/c$. To remove τ pairs, events with three tracks inside an 11° opening angle around the thrust axis were rejected. The main background after this selection is from four-fermion processes.

For the channel with no missing energy at least two tracks with the same charge were required to be identified as electrons or muons in order to reject $e^+e^-\pi^+\pi^-$ events and $\gamma\gamma$ processes to $\pi^+\pi^-\pi^+\pi^-$ and $\tau^+\tau^-$. Because of leptonic number conservation, the flavour of all the tracks can be deduced if the two tracks with the same charge are identified as two electrons or two muons. In the $e^+\mu^+$ and $e^-\mu^-$ cases, a third identified track was required, otherwise the event was rejected.

Then for each event, the invariant masses of combinations of two tracks with opposite electric charge were reconstructed. The smallest invariant mass, $m_{\ell\ell}$, and the largest one, $M_{\ell\ell}$, only were considered and events with $m_{\ell\ell}$ less than $1.8 \text{ GeV}/c^2$ or $M_{\ell\ell}$ greater than $80 \text{ GeV}/c^2$ were rejected. For each event, the visible energy, E_{vis} , and the missing momentum, p_{miss} , were reconstructed and the following conditions applied: $0.92\sqrt{s} < E_{\text{vis}} + p_{\text{miss}} < 1.08\sqrt{s}$, $E_{\text{vis}} > 0.6\sqrt{s}$ and $p_{\text{miss}} < 0.4\sqrt{s}$. For each event surviving these cuts all four combinations of three-track invariant masses were computed. This reconstruction, constrained by energy and momentum conservation, leads to a mass resolution of $300 \text{ MeV}/c^2$ for signal events, independent of mass. The flavour of the excited lepton is determined by the lepton recoiling against the three tracks used to reconstruct the invariant mass. In the search for single production of excited electrons a cut $|\cos\theta| < 0.8$ was finally applied on the recoiling electron to minimize t -channel effects.

The numbers of e^*e and $\mu^*\mu$ candidates are 14 and 23 respectively, while 19.6 and 26.8 are expected from four-fermion channels with other backgrounds negligible. Fig. 7 shows the reconstructed mass distribution for data and background; there is good agreement between the two.

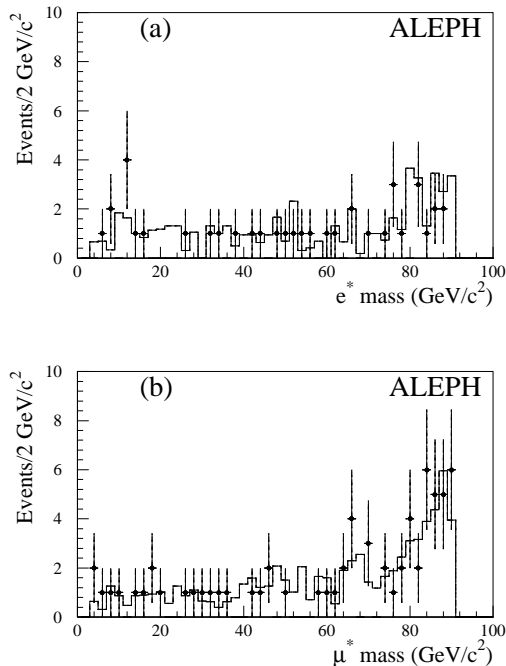


Figure 7: Distribution of the reconstructed excited lepton mass in the four-prong final state: (a) excited electron; (b) excited muon. The histograms show the background distribution and the points the candidate event contributions.

In the search for four-prong events with missing energy, at least two of the four tracks were required to be identified as leptons, independent of their charge. Cuts on invariant masses reconstructed from pair combinations were again applied, with the cut kept at $1.8 \text{ GeV}/c^2$ for $m_{\ell\ell}$ and decreased to $56 \text{ GeV}/c^2$ for $M_{\ell\ell}$. Events with a total energy outside the range 20 to 88 GeV were rejected. These criteria selected 17 candidates with 16.0 background events predicted. For processes where the lepton in the final state is a direct decay product of the excited lepton candidate, lepton identification was performed.

Requiring at least one electron, two electrons, one muon, and two muons, the number of candidates reduced to 12, 6, 12 and 7 respectively, while 12.7, 7.5, 10.1 and 4.9 background events were predicted.

The efficiency for the channels with no missing energy varies from 30% to 45% for $\mu^*\mu$ while it is lower for e^*e , mainly due to the $\cos\theta$ cut. For $\tau^*\tau$ the efficiency was deduced from the four track analysis with missing energy, but the τ^* mass can no longer be reconstructed. The efficiency is of the order of 20% — smaller than for the muon since both taus have to decay into one prong and lepton identification is imposed. The efficiencies for pair production increase with mass. For e^* , μ^* , ν_e^* , and ν_μ^* , they are between 30% and 50%, while for τ^* and ν_τ^* they are in the range 20% – 40%.

5.1.3 Search for six-prong final states

This analysis searches for pair production of e^* and μ^* , followed by NC decays into charged leptons to produce six charged tracks with zero total charge and no neutral clusters. Two kinematic cuts were applied: (i) the thrust was required to be less than 0.98 to reject residual background from Z decays into two jets and τ pairs and (ii) the scalar sum of the momenta was required to be larger than $0.75\sqrt{s}$ to reject residual τ pairs in which the final state includes at least two neutrinos and large missing energy.

These two cuts lead to a signal efficiency for $e^*\bar{e}^*$ varying from 30% to 40%, while for $\mu^*\bar{\mu}^*$ it ranges from 40% to 50%. After applying the cuts to the whole data sample and to background simulations no candidate remained in either case.

5.2 Search for hadronic final states

Searches for single production, followed by hadronic decays, have been made in the e^*e , $\nu^*\nu$ and $\mu^*\mu$ channels. Depending on the charge of the excited lepton and its decay mode (CC or NC), three configurations of final states can be produced: hadrons only plus missing energy; an $\ell^+\ell^-$ pair plus hadrons; one charged lepton, hadrons and missing energy (Table 3). Separate searches have been carried out for these three configurations.

Channel	Weak decay	Final state topology	Missing energy?
$\nu^*\nu$	$\nu\nu Z$	$q\bar{q}\nu\bar{\nu}$	Yes
$\nu^*\nu$	$\ell\nu W$	$q\bar{q}'\ell\nu$	Yes
$\ell^*\ell$	$\ell\ell Z$	$q\bar{q}\ell^+\ell^-$	No
$\ell^*\ell$	$\ell\nu W$	$q\bar{q}'\ell\nu$	Yes

Table 3: Possible hadronic states in weak decays of excited leptons.

Three processes contribute significant backgrounds, the degree of contamination depending strongly on the excited lepton mass m^* : (i) $e^+e^- \rightarrow q\bar{q}$, which contaminates the high mass candidates; (ii) $e^+e^- \rightarrow \tau^+\tau^-$, which mainly contaminates the low mass candidates; (iii) four-fermion final states $e^+e^- \rightarrow \ell\bar{\ell}q\bar{q}$ or $\nu\bar{\nu}q\bar{q}$.

5.2.1 Common kinematic properties of hadronic final states

Since signal events produce an energetic charged lepton or neutrino, hadronic backgrounds with leptonic decays of heavy quarks have been greatly reduced with an energy cut of 5 GeV on the charged lepton energy. The same cut has been applied to the energetic neutrino, defined by the missing momentum.

For a given ℓ^* mass, the hadronic mass spectra from CC or NC decays are very similar. The following cuts were therefore applied to the hadronic system after excluding the energetic charged lepton(s): track multiplicity greater than two; charged energy between 5 and 50 GeV; total energy less than 70 GeV and transverse momentum greater than 10 GeV.

At low ℓ^* mass the lepton recoiling against the ℓ^* is usually located in one hemisphere and the charged tracks from the ℓ^* decay are in the other (the hemispheres being defined by a plane perpendicular to the thrust axis). At high ℓ^* mass the charged tracks are distributed more uniformly. Thus, after excluding the energetic lepton(s), two event configurations were defined: (i) a low mass configuration ($< 30 \text{ GeV}/c^2$) with $N_{\text{ch}} \geq 3$, $E_{\text{ch}} \geq 5 \text{ GeV}$ and all tracks in one hemisphere, the fraction of the visible energy in a small angle around the beam axis ($|\cos \theta| \geq 0.75$) not exceeding 65%; (ii) a high mass configuration ($> 30 \text{ GeV}/c^2$) with $N_{\text{ch}} \geq 5$, $E_{\text{ch}} \geq 10 \text{ GeV}$ and charged tracks distributed in both hemispheres. These two sets of cuts are exclusive and the global efficiency for an ℓ^* signal is the sum of the two separate efficiencies.

5.2.2 Final states with hadrons, missing energy and no leptons

In the low mass configuration the main background arises from $\tau^+\tau^-$ events with an unreconstructed charged track in one hemisphere. This background was reduced by two further cuts: the maximum angle between two charged tracks was required to be greater than 10° , and the neutral energy in the empty hemisphere less than 3 GeV. After these cuts, 11 events remain in the data while 9.9 τ pair events are expected.

In the high mass configuration, the main background comes from hadronic Z decays. A signal event is characterized by the emission of two neutrinos, i.e. by missing energy and missing transverse momentum, so two-jet or three-jet events were selected using the JADE algorithm with $y_{\text{cut}} = 0.03$ in order to discriminate ν^* jets from background jets. The jets in a two-jet signal event are acollinear and acoplanar. The acollinearity angle was therefore required to be smaller than 150° , the acoplanarity angle less than 160° and the thrust value less than 0.93. A last cut, on the minimum angle, θ_{min} , between the missing momentum and the nearest jet, was applied at 60° . For three jets coming from ν^* , the emission of neutrinos makes the sum, Σ , of the angles between each pair of jets smaller than 360° , while the similar sum for background events is peaked at 360° . The following requirements were applied: $\Sigma \leq 350^\circ$, the maximum angle between two jets less than 160° and θ_{min} larger than 60° . Combining the two-jet and three-jet analyses, 12 candidates remain, the expected background being 8.3.

By adding the results of low mass and high mass analyses, the final efficiency for the ν^* signal is around 70% in the mass range 10 to 80 GeV/c^2 .

5.2.3 Final states with two charged leptons and hadrons

The analysis for this channel is identical for both e^*e and $\mu^*\mu$ NC decays. The main backgrounds are $\tau^+\tau^-$ and $q\bar{q}$ events, and the four-fermion processes $e^+e^- \rightarrow \ell\bar{\ell}q\bar{q}$ with two energetic charged leptons.

In the low mass configuration, e^*e and $\mu^*\mu$ signal events have one lepton in one hemisphere and the second lepton with all other charged tracks in the second hemisphere. The following kinematic cuts were applied: the total energy of the two leptons was required to be greater than 35 GeV, the invariant mass of all objects included in the second hemisphere to be larger than $5 \text{ GeV}/c^2$. In addition geometric cuts were applied so that the maximum angle between a charged track and the thrust axis had to be larger than 12° and the angle between the two leptons to be larger than 20° . After these cuts, 11 e^*e candidates remained while 11.1 $e\bar{e}$ background events are expected. For the $\mu^*\mu$ channel, 11 candidates remained while 10.7 $\mu\bar{\mu}$ background events are expected.

In the high mass configuration a jet analysis was again performed after removing the energetic leptons. Kinematic cuts were made requiring the total energy of the leptons to be greater than 30 GeV and the invariant mass of one lepton with each jet to be larger than $12 \text{ GeV}/c^2$ for two-jet events and $8 \text{ GeV}/c^2$ for three-jet events. Finally, requiring the two lepton invariant mass to be larger than $4 \text{ GeV}/c^2$ rejected $q\bar{q}$ events with two semileptonic (cascade) decays in the same jet. The observed and expected numbers of events were respectively 6 and 4.1 for the e^*e search, and 5 and 3.3 for the $\mu^*\mu$ search.

Combining the high and low mass analyses gives an efficiency for both the e^*e and the $\mu^*\mu$ channel which varies from 40% to 50% over the ℓ^* mass range.

5.2.4 Final states with one charged lepton, one neutrino and hadrons

In CC processes, an energetic neutrino is emitted. Setting the neutrino energy, E_ν , equal to the magnitude of the missing momentum, $E_\nu > 5 \text{ GeV}$ was required and the angle of the missing momentum with the beam direction was required to exceed 18° . Defining $r_\nu = E_\nu/E_{\text{miss}}$, with E_{miss} the missing energy, the requirement $0.4 < r_\nu < 1.6$ was applied removing most of the $\tau^+\tau^-$ and $q\bar{q}$ backgrounds with one lepton candidate.

The kinematic and geometric cuts described in Section 5.2.3 were used for this search with the neutrino now playing the role of a charged lepton. All cuts were applied with the same values, except for the lepton-neutrino invariant mass cut which was increased to $7 \text{ GeV}/c^2$ in the high mass configuration.

In the low mass configuration the number of observed events in the e^*e search is 11 while the expected background is 8.4. For $\mu^*\mu$, 3 events are observed and 8.8 background events are expected. In the high mass configuration, the observed and expected background numbers are 15 and 14.8 for the e^*e search, and 14 and 16.5 for $\mu^*\mu$. The signal efficiencies vary with mass from 35% to 60%, independent of ℓ^* flavour.

5.2.5 Invariant mass reconstruction

In the case where two charged leptons are identified, the masses of excited lepton candidates can be reconstructed either directly as the invariant mass of one of the two leptons with the hadrons, or as the recoil mass to the other lepton. The same procedure has been applied in the case of one charged lepton and one neutrino. Signal simulations show that the first method is more accurate at low mass, while the second is better at

high mass. The invariant mass of a candidate has been taken as the weighted average of the two and the mass resolution is typically $10 \text{ GeV}/c^2$ [39]. The mass spectra for data and background are in agreement.

5.3 Combination of limits

From the results presented in the preceding sections, limits on compositeness parameters for different decay topologies have been established separately for both single and pair production of excited leptons. In the following, limits based on a combination of all the available topologies are presented. For single production these are combined in two stages: the separate channels (leptonic and hadronic) from the NC and CC modes are combined separately; then a full combination of all channels, including radiative decays, is made.

In the case of pair production, where only leptonic final states are studied, separate combinations are made for channels coming respectively from double NC, double CC and mixed modes (ZZ, WW, WZ); again full combinations are performed for the three modes and the radiative one.

In order to combine channels, a probability distribution function for s events has been defined as the product of separate Poisson distributions for each decay channel i [40]

$$D(s) = \prod_i P(n_i, p_i s + b_i) \quad (4)$$

where p_i is the relative weight of the channel, given by $p_i = \epsilon_i \text{BR}_i / \sum_j \epsilon_j \text{BR}_j$, ϵ_i being the detection efficiency, and BR_i being the branching ratio for the decay $Z (W) \rightarrow f_i \bar{f}_i$; n_i and b_i are the number of observed events and predicted background events respectively.

The total number of signal events, s , expected for given values of the compositeness parameters includes all channels mediated by a virtual Z (W). From the 95% c.l. upper limits on s obtained in the two cases, corresponding limits on the compositeness parameters have been obtained. This procedure has been applied in order to combine topological limits for pair production (Figs 8 and 9) and single production (Figs 10 and 11) assuming the known branching ratios of the Z (W). In the case of single production, because of the large hadronic branching ratios (70%) and their good efficiencies (around 50%), the combined limits are very close to those estimated from the hadronic final states alone.

The same method has been applied to combine the radiative, the NC and the CC decay channels with weights determined from the model of ref. [35]. Two sets of values of the parameters f and f' in equation 2 are particularly significant in this model — $f = f' = 1$ and $f = 1, f' = -1$. In the first case, radiative decays of the excited neutrinos are forbidden and only weak decays are allowed, dominated by the CC decay which represents more than 75% in the mass range $10 - 80 \text{ GeV}/c^2$. For excited charged leptons the radiative decay is close to 100%. In the second case the ℓ^* radiative decay is forbidden and only the weak decays remain; the CC branching ratio dominates, varying from 73% to 86% in the mass range $10 - 80 \text{ GeV}/c^2$. For ν^* the radiative decay dominates and is very close to 100% over the whole mass range. However as soon as f and f' vary by just a small amount from these limiting cases radiative decays dominate all channels. For example if $f = 1.025$ and $f' = 0.975$ the ν^* branching ratios change completely so that

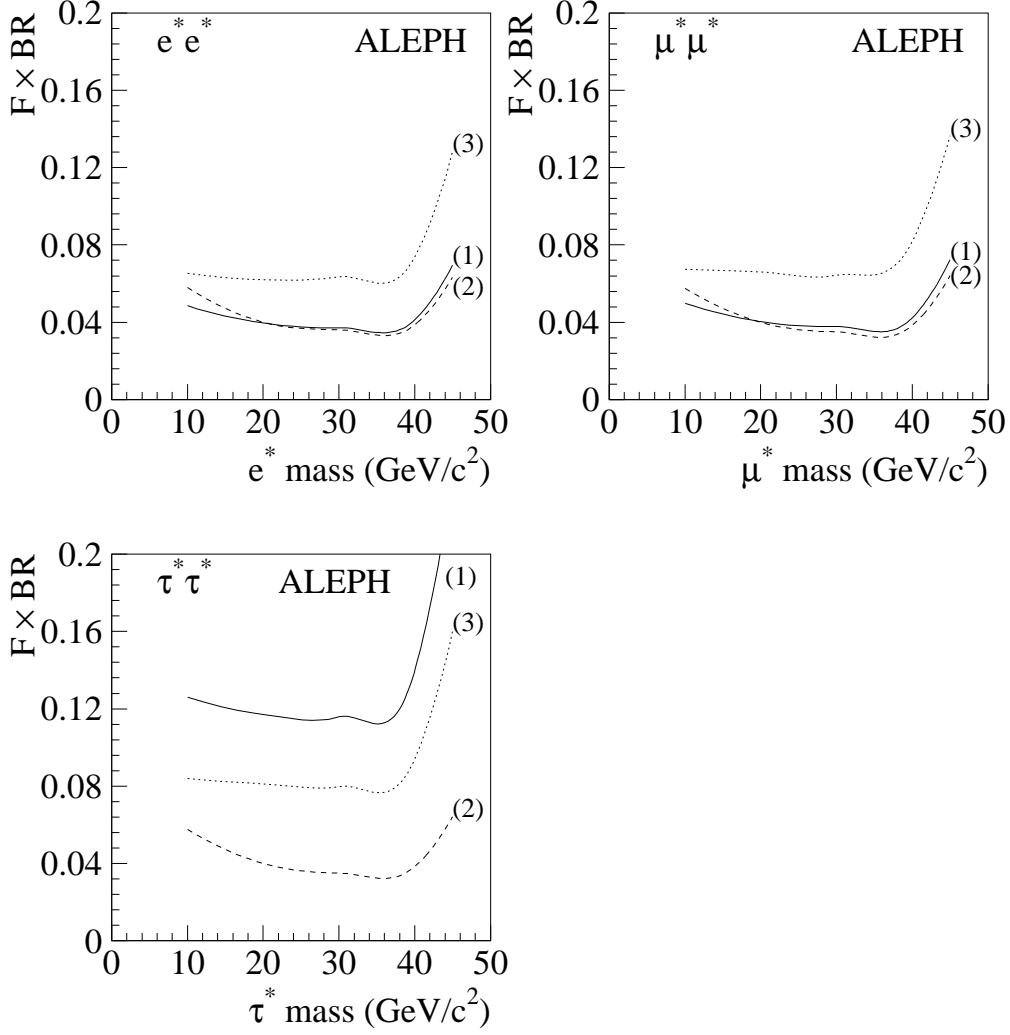


Figure 8: Form factor times branching ratio limits in ℓ^* double production. Curves (1), (2) and (3) show limit combinations for $\ell\ell ZZ$, $\nu_\ell \nu_\ell WW$ and $\nu_\ell \ell WZ$ decays ($\ell = e, \mu, \tau$) respectively. For curve (1) $BR \equiv BR(\ell^* \rightarrow \ell Z)$; for curve (2) $BR \equiv BR(\ell^* \rightarrow \nu_\ell W)$; for curve (3) $BR \equiv \sqrt{2BR(\ell^* \rightarrow \ell Z)BR(\ell^* \rightarrow \nu_\ell W)}$.

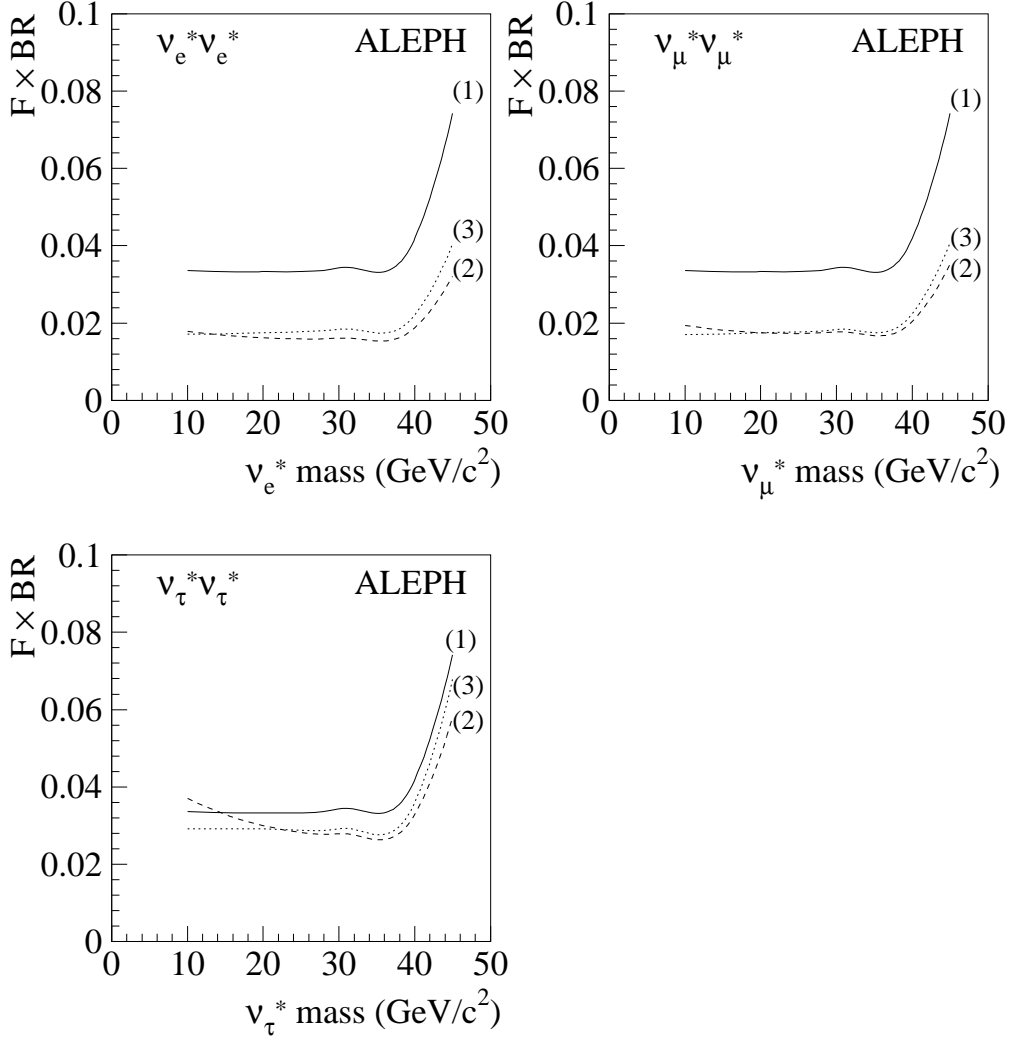


Figure 9: Form factor times branching ratio limits in ν^* double production. Curves (1), (2) and (3) show limit combinations for $\nu_\ell \nu_\ell ZZ$, $\ell\ell WW$ and $\ell\nu_\ell WZ$ decays ($\ell = e, \mu, \tau$) respectively. For curve (1) $BR \equiv BR(\nu^* \rightarrow \nu_\ell Z)$; for curve (2) $BR \equiv BR(\nu^* \rightarrow \ell W)$; for curve (3) $BR \equiv \sqrt{2BR(\nu^* \rightarrow \ell W)BR(\nu^* \rightarrow \nu_\ell Z)}$.

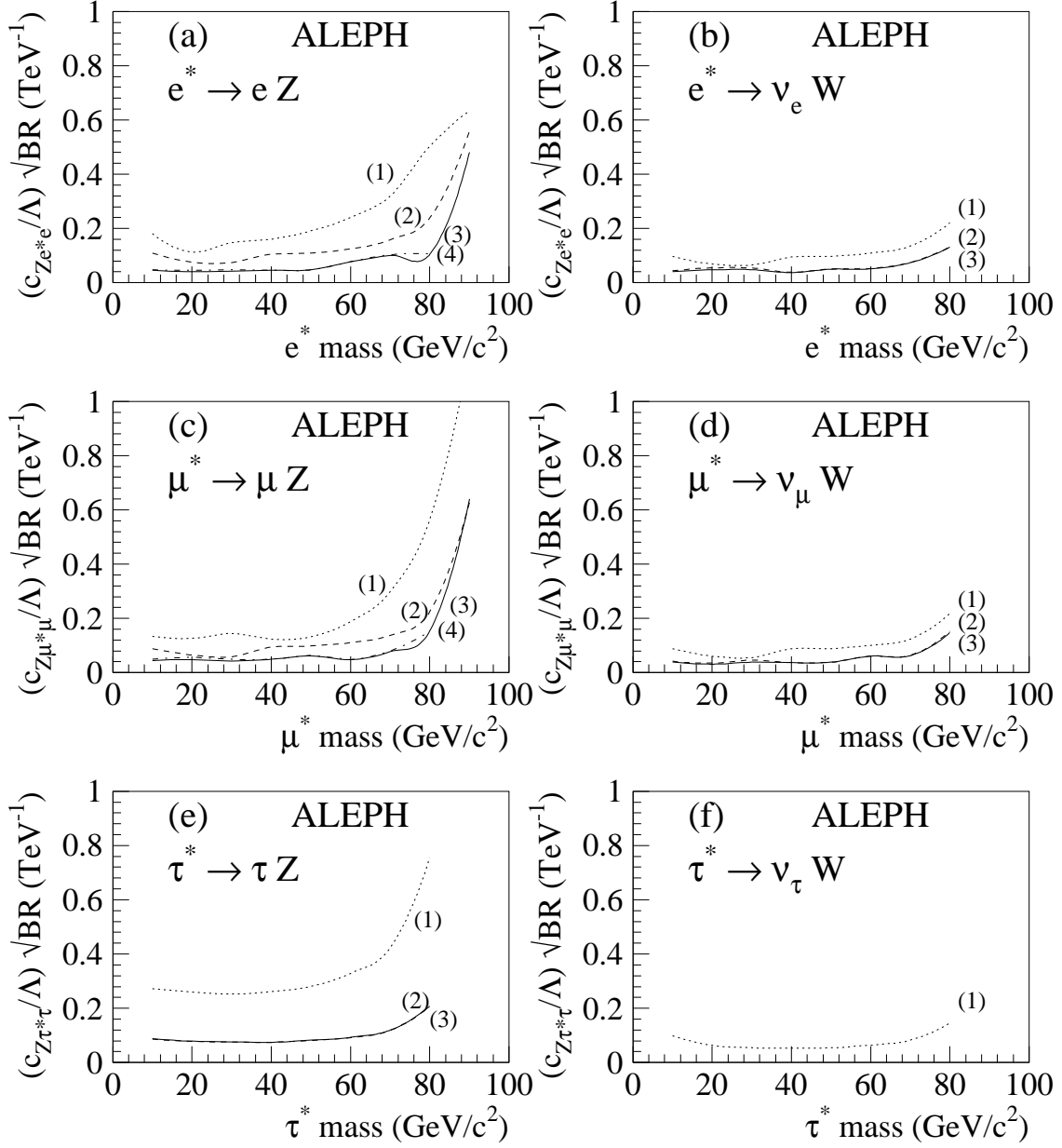


Figure 10: Coupling times branching ratio limits for e^* , μ^* and τ^* single production. (a) e^* NC decay: (1) $e(\ell\bar{\ell})$, (2) $e(\nu\bar{\nu})$, (3) $e(q\bar{q})$, (4) combined limit. (b) e^* CC decay: (1) $\nu_e(\ell\nu_\ell)$, (2) $\nu_e(q\bar{q}')$, (3) combined limit. (c) μ^* NC decay: (1) $\mu(\ell^+\ell^-)$, (2) $\mu(\nu\bar{\nu})$, (3) $\mu(q\bar{q})$, (4) combined limit. (d) μ^* CC decay: (1) $\nu_\mu(\ell\nu_\ell)$, (2) $\nu_\mu(q\bar{q}')$, (3) combined limit. (e) τ^* NC decay: (1) $\tau(\ell^+\ell^-)$, (2) $\tau(\nu\bar{\nu})$, (3) combined limit. (f) τ^* CC decay: (1) $\nu_\tau(\ell\nu_\ell)$.

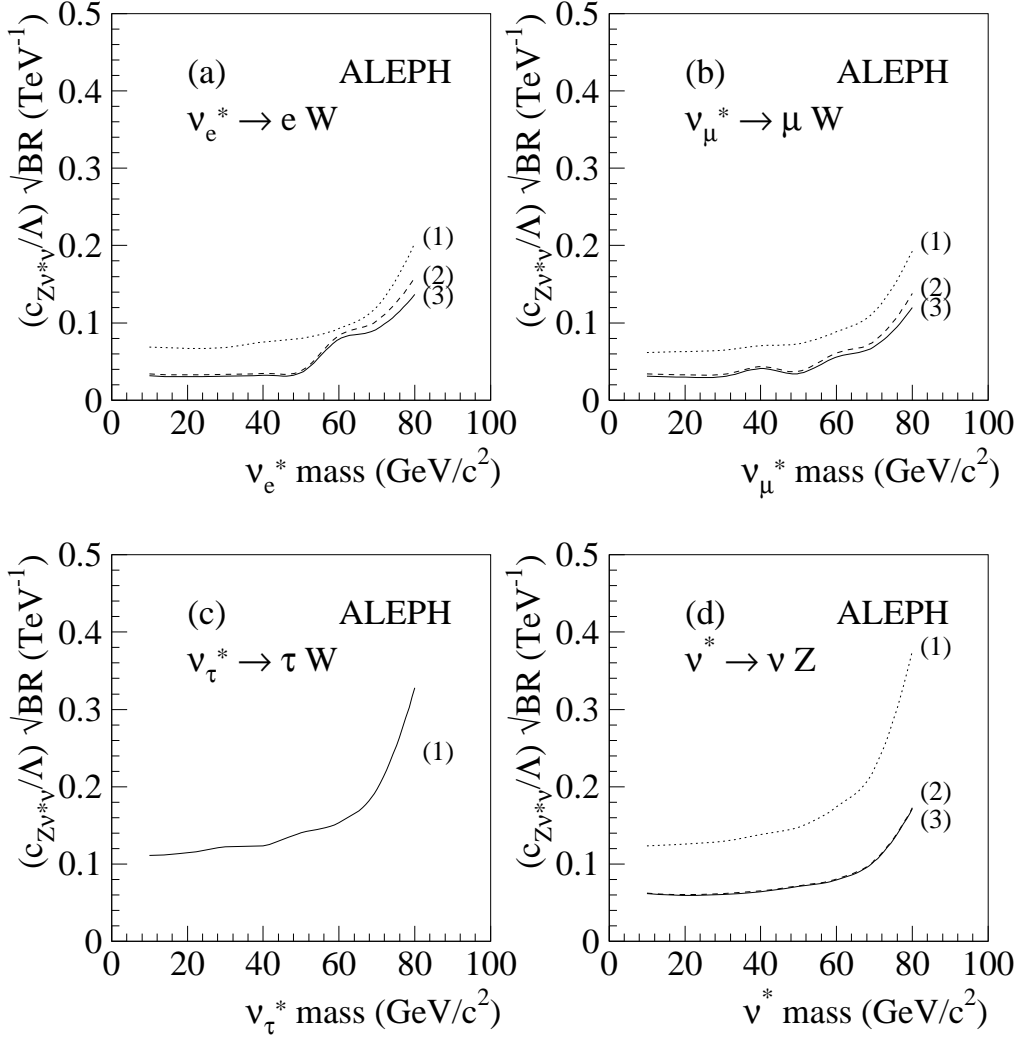


Figure 11: Coupling times branching ratio limits for ν^* single production (a) ν_e^* CC decays: (1) $e(\ell\nu_\ell)$, (2) $e(q\bar{q}')$, (3) combined limit. (b) ν_μ^* CC decays: (1) $\mu(\ell\nu_\ell)$, (2) $\mu(q\bar{q}')$, (3) combined limit. (c) ν_τ^* CC decays: (1) $\tau(\ell\nu_\ell)$. (d) ν^* NC decays: (1) $\nu(\ell^+\ell^-)$, (2) $\nu(q\bar{q})$, (3) combined limit.

$\text{BR}(\nu^* \rightarrow \nu + \gamma)$ is greater than 92% for m_{ν^*} less than $30 \text{ GeV}/c^2$, decreasing progressively to 5% at $80 \text{ GeV}/c^2$.

The model allows limits to be set on the two ratios $c_{Z\ell^*\ell}/\Lambda$ and $c_{Z\nu^*\nu}/\Lambda$ as a function of f and f' for the three flavours of ℓ^* and ν^* . The two specific cases mentioned above are shown in Figs 12 and 13. The limits range respectively from 0.04 TeV^{-1} to 0.28 TeV^{-1} in the ℓ^* channels and from 0.036 TeV^{-1} to 0.36 TeV^{-1} in ν^* .

Limits can also be found on the substructure energy scale, Λ . The pairs of values for f and f' considered above give $c_{Z\ell^*\ell} = 0.32$ and 0.59 , and $c_{Z\nu^*\nu} = 0.59$ and 0.32 respectively, leading to lower limits on Λ as also shown in Figs 12 and 13. They vary from 1.4 to 16 TeV for charged excited leptons and from 3.2 to 16.5 TeV for excited neutrinos.

The form factor limits for $\ell^*\bar{\ell}^*$ and $\nu^*\bar{\nu}^*$ production are shown in Fig. 14. In the mass range $10 - 40 \text{ GeV}/c^2$, they vary from 0.005 to 0.08 in the $\ell^*\bar{\ell}^*$ channels and from 0.004 to 0.05 in the $\nu^*\bar{\nu}^*$ channels. For a mass close to $45 \text{ GeV}/c^2$, which is the upper kinematic bound, form factor limits increase rapidly.

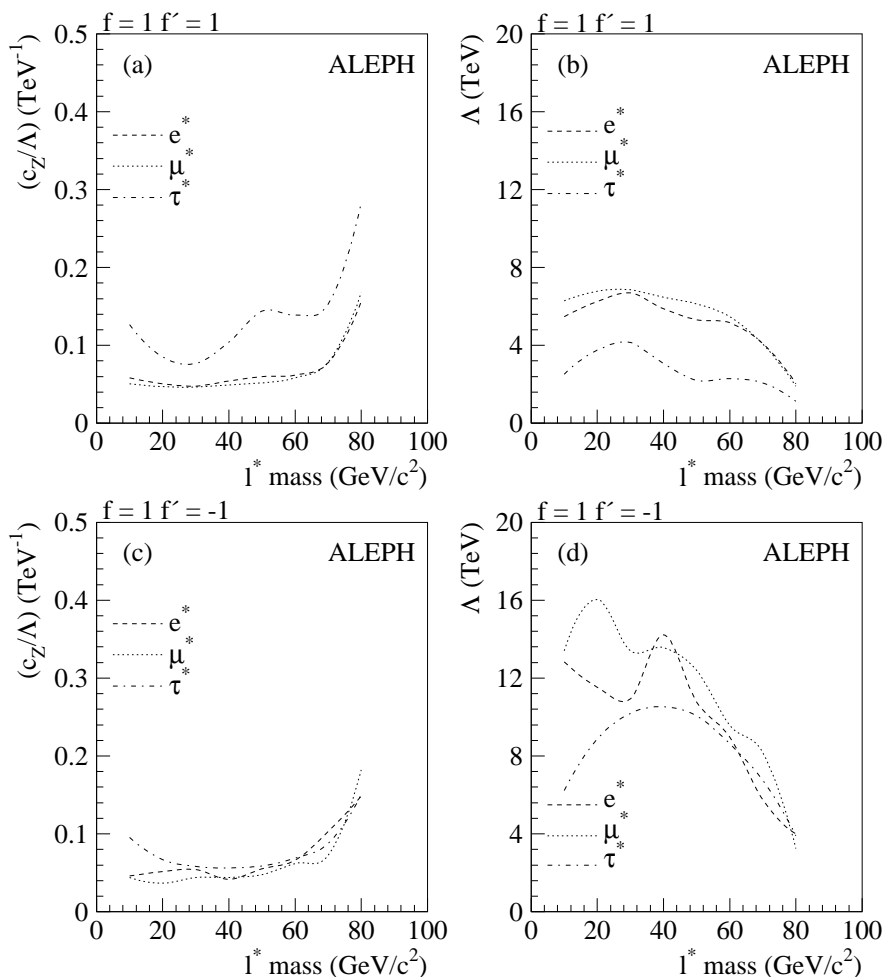


Figure 12: Compositeness limits at 95% c.l. for excited charged lepton production assuming the given values for f and f' . (a) and (c) are the upper limits on c_Z/Λ , (b) and (d) are the lower limits on the compositeness energy scale.

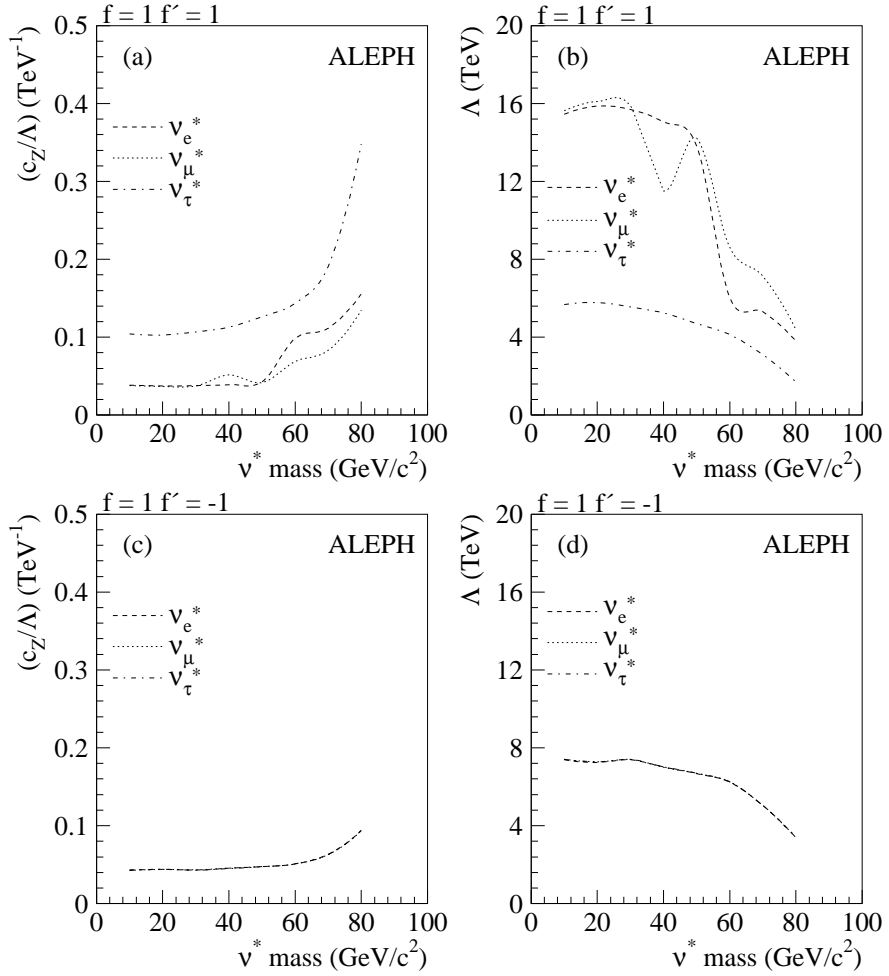


Figure 13: Compositeness limits at 95% c.l. for excited neutrino production assuming the given values for f and f' . (a) and (c) are the upper limits on c_Z/Λ , (b) and (d) are the lower limits on the compositeness energy scale.

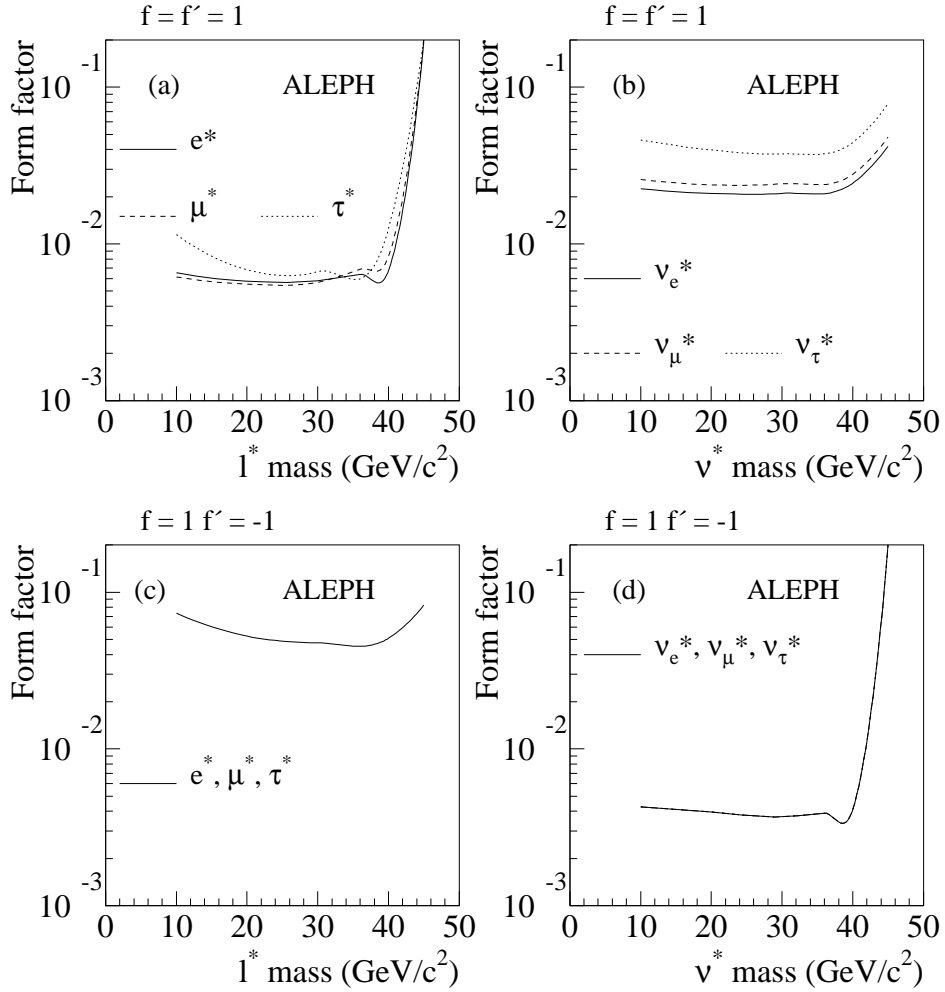


Figure 14: Upper limits at 95% c.l. on pair production form factors assuming the given values for f and f' .

5.4 Summary

No evidence for weak decays of excited leptons has been found and stringent coupling limits have been set. By combining radiative, CC and NC channels, a mass dependent lower limit on the compositeness energy scale, Λ , of up to 16 TeV is deduced, confirming the hypothesis that leptons are point-like at LEP 1 energies.

Coupling limits for weak decays of excited leptons have been reported at higher LEP energies [17,28,30,32], and for weak decays of e^* and ν^* in the mass range 100 – 250 GeV/ c^2 at HERA [33,34].

6 The search for excited quarks

The existence of excited quarks is expected in many composite models. Their couplings may be the same as standard quarks or may be modified by form-factors [41]. Deexcitation is *via* $q^* \rightarrow q + \gamma$ and $q^* \rightarrow q + g$, with branching ratios that are model dependent; in the absence of any special constraints the gluonic decay has been estimated to be about 90% [42].

In order to set mass limits it is assumed that cross-sections for pair production are given by the Standard Model. In addition, form factor limits are derived for lower masses. Below about 10 GeV/ c^2 the topology of events arising from q^* production is very similar to $q\bar{q}$ and in this region limits have been derived from the Z hadronic width.

For single production, $e^+e^- \rightarrow q^*q$, the Lagrangian assumed is an adaptation of the one described in Section 1, with a colour factor and a gluon interaction term added [43]. The latter does not contribute to the production process, but provides the “gluonic” decay mode.

The results previously published by ALEPH [16] were based on a small part of the present data. There unit form factor had been assumed for pair production and only masses above 40 GeV/ c^2 had been considered for single production.

6.1 The decay $q^* \rightarrow q + g$

Separate searches have been carried out for single and pair production, the backgrounds being the QCD processes $q\bar{q}g$, $q\bar{q}gg$, $q\bar{q}q\bar{q}$, which were simulated using JETSET 7.3 [44]. Monte Carlo signal events were generated with a modified version of this generator in which q^* generation is followed by the decay $q^* \rightarrow q + g$, then by parton showering from quarks and gluons.

The $q^*\bar{q}^*$ analysis was based on the search for four-jet events in which the jets can be assigned to two dijet subsystems which are similar in topology and invariant mass. Events were discarded if they had aplanarity less than 0.02 or thrust above 0.925 (for q^* masses below 20 GeV/ c^2 these cuts were changed to 0.01 and 0.95 respectively). The remaining events were forced into a four-jet configuration using the JADE cluster algorithm and any event in which a jet had fewer than three charged tracks was discarded. The jet energies were rescaled using energy and momentum conservation and the dijet invariant masses for the three dijet pairings were computed. The combination with the lowest mass difference was chosen and the mass difference was required to be less than 15 GeV/ c^2 . The difference in opening angles between the two jets forming each q^* candidate was required to be less than 45° (increased to 90° for masses below 20 GeV/ c^2). The decay angles θ_1^d and θ_2^d ,

defined as the acute angle measured in the rest frame of each q^* between the direction of the q^* and the back-to-back jet pair, had to satisfy $\cos \theta_1^d \cos \theta_2^d < 0.9$. With these cuts the signal efficiency is 58% for a q^* mass between 40 and 44 GeV/c^2 , but decreases with decreasing mass. The modifications to the cuts in the low mass region increase the efficiency by about 30%. The variation in efficiency with quark flavour is small. The resolution on the dijet mass sum varies between 1.7 and 2.1 GeV/c^2 over the mass range and is about 6 GeV/c^2 on the dijet mass difference. Fits were made to the distribution of the dijet mass difference for successive bins of the average dijet mass 7 GeV/c^2 wide, moved in 1 GeV/c^2 steps. A sum of background and signal Monte Carlo distributions was fitted to the data and the signal fraction in each mass bin was determined. The data contain no evidence for a q^* signal and limits have been set on the form factor times the branching ratio to qg , assuming the existence of a single excited u-type quark (the most conservative assumption). These limits are shown in Fig. 15(a).

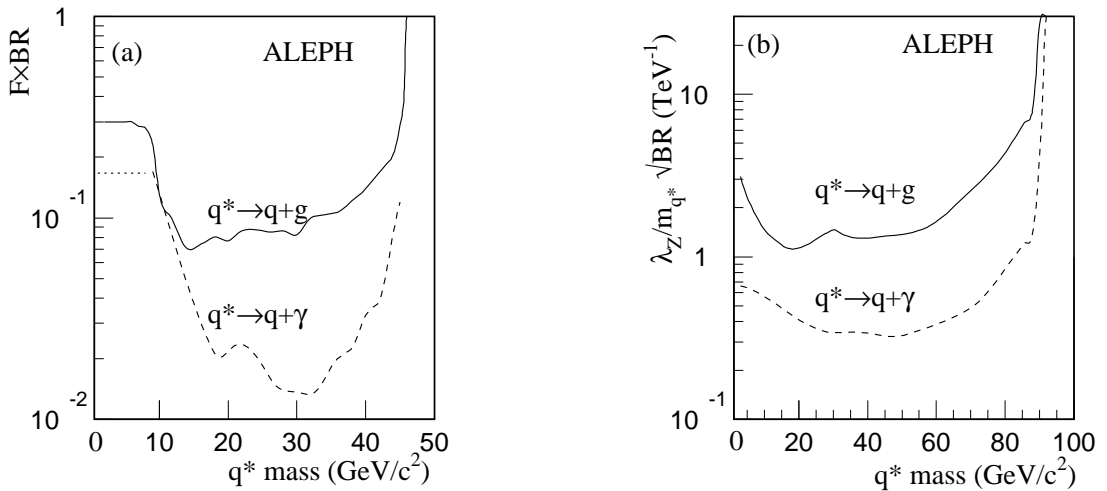


Figure 15: (a) Form factor times branching ratio limits at 95% c.l. for $q^* \bar{q}^*$ production for gluonic and photonic decay. (b) Single q^* production: 95% c.l. upper limits on $\lambda_Z/m_{q^*} \sqrt{BR}$ for $q^* \rightarrow q + \gamma$ and $q^* \rightarrow q + g$.

The $q^* \bar{q}^*$ analysis was based on events with thrust less than 0.925. Such events were forced into a three-jet configuration and those in which the lowest energy jet did not contain a charged track or in which either of the other two jets did not have at least three charged particles were rejected. The efficiency for Monte Carlo signal is around 70% over most of the mass range, decreasing rapidly below 20 GeV/c^2 and above 80 GeV/c^2 to around 20%. The jets were projected onto the plane defined by the thrust and major axes (the event plane) and then rescaled using energy and momentum conservation. The dijet invariant masses and the corresponding decay angles, θ^d , were computed for the three combinations of jet pairs. The highest mass combination was omitted in searches for q^* masses below 50 GeV/c^2 and the lowest mass combination was omitted for searches above 80 GeV/c^2 . Fits were made to the $\cos \theta^d$ distribution for sliding mass bins of 15 GeV/c^2 and hence limits derived for $\lambda_Z \sqrt{BR}/m_{q^*}$ as a function of mass assuming production of a single excited quark, where BR is the branching ratio for $q^* \rightarrow q + g$ (Fig. 15(b)).

6.2 The decay $q^* \rightarrow q + \gamma$

The background in this channel is radiative $q\bar{q}$ production, $Z \rightarrow q\bar{q}\gamma$, with either initial or final state radiation. Both isr and fsr photons tend to have low energy, and fsr photons are usually close to their parent particles, so that background is readily distinguished from signal.

The $q^*\bar{q}^* \rightarrow q\bar{q}\gamma\gamma$ analysis followed that of the gluonic channel until four jets had been found, but omitted the aplanarity cut. It was then required that one jet has at least four charged tracks, another at least two, and that the other two have at least 90% of their energy due to one identified photon and have no charged particle above 0.5 GeV within 30° of the photon (for q^* masses below 20 GeV/ c^2 this was reduced to 15°). After energy rescaling the invariant masses for the jet-photon combinations were calculated and again the lower mass difference was required to be less than 15 GeV/ c^2 . The same variables and cuts were then used as in the gluonic channel. The efficiency is around 40% for masses above 20 GeV/ c^2 , but falls sharply to 2% at 10 GeV/ c^2 . A very important source of events in this channel is expected to be second order isr, but this was not included in the background simulation. Accordingly only 46.6 events were predicted, whereas 98 were found in data, but there was no evidence for any preferred mass, so limits were set by using the factor $\exp(-(\Delta M_{\text{jet},\gamma}/\sigma)^2)$ to weight the events in favour of equal mass candidates, where σ is the resolution on the mass difference ΔM . The resultant mass plot was fitted for maximal signal permitted by the data and background, with the background normalization factor allowed to float in the fit. The form factor times the branching ratio limit is shown in Fig. 15(a). For $m_{q^*} < 10$ GeV/ c^2 the sensitivity of the direct searches is poor because of merging of the jets from the q^* decay. Where the limit derived from the measured Z hadronic width (Appendix A) is better this has been used and displayed on the figure.

For single production, $q\bar{q}\gamma$ events form a significant background. After three-jet reconstruction of the event, one jet was required to contain at least four charged tracks, another at least two, and the third to satisfy the photon criteria described above. Energy rescaling was applied and the two possible jet-photon invariant masses were calculated. Signal efficiency is low at q^* masses close to the Z mass since the two jets frequently overlap, and thus two-jet events in which one jet was an energetic photon, were also selected. In this case the invariant mass was set to the centre of mass energy. Fits were made to the photon energy distribution in different bins of jet-photon invariant mass with two entries per event. The coupling limits derived are shown in Fig. 15(b).

Finally, assuming that the sum of the gluonic and photonic branching ratios is unity, limits can be set on the form factor, F , for $q^*\bar{q}^*$ production and the coupling λ_Z/m_{q^*} for single q^* production, independent of the individual branching ratios. In both cases these branching ratio independent limits are very close to the $q^* \rightarrow q + g$ limits (with BR= 1) plotted in Fig. 15 and are not shown.

6.3 Summary

No evidence has been found for production of excited quarks. The search for pair production has allowed mass limits for Standard Model couplings to be set at 45 GeV/ c^2 , while for lower masses form factor limits have been set which depend on the assumed decay mode. For single production, limits have been set on the parameter λ/m_{q^*} for

masses up to $85 \text{ GeV}/c^2$, again dependent on the decay mode. Other LEP collaborations have also published limits on some of these processes [45, 46]. Limits on excited quark production have also been established at ep [33, 34] and $p\bar{p}$ [47, 48] colliders but their sensitive mass range is generally above that covered here.

7 Search for the decay Z to γS

In models in which the Z is composite it is expected to decay to the scalar (S) combination of the same preonic constituents plus a photon, provided that $m_S < m_Z$. Although similar to the Higgs, S would have different couplings. Taking the value of an effective subconstituent mass to be 1 TeV , Γ_S is $\mathcal{O}(\text{few MeV})$, significantly smaller than the detector resolution on the mass of the S . If the preonic constituents are coloured then a larger width could be expected, but Γ_S is still likely to be small [49].

The decays of the S considered here are $\ell^+\ell^-$, $q\bar{q}$, gg , $\gamma\gamma$ and $\nu\bar{\nu}$. A Higgs boson generator [50] was used for signal Monte Carlo. Events were produced with both negligible width and with a width equal to $0.05m_S$ at $5 \text{ GeV}/c^2$ mass intervals up to $80 \text{ GeV}/c^2$, then at $1 \text{ GeV}/c^2$ intervals above this.

The searches in the $\ell^+\ell^-\gamma$, $gg\gamma$ and $q\bar{q}\gamma$ channels used similar cuts to those described earlier for ℓ^* and q^* radiative decays. The only significant change was the extension of the photon energy range down to 3 GeV in order to increase the mass reach for the S . Where there was more than one photon in an event the most energetic was assumed to originate from the Z decay.

In the $\ell^+\ell^-\gamma$ channel the final sample contains 6787 $e^+e^-\gamma$ events, 4469 $\mu^+\mu^-\gamma$ events and 3309 $\tau^+\tau^-\gamma$ events, compared to 6616, 4515 and 3183 predicted from radiative electroweak processes. Contamination from other processes is negligible, but some electron and muon events appear in the tau channel. Signal efficiencies are 65% and above in the $e^+e^-\gamma$ and $\mu^+\mu^-\gamma$ channels, and 45% in the $\tau^+\tau^-\gamma$ channel.

In the $q\bar{q}\gamma$ and $gg\gamma$ channels too many signal events are lost by the photon isolation cut at masses above $80 \text{ GeV}/c^2$ where the jets are back-to-back and the photon is soft, and it was reduced to 15° in this mass region. Signal efficiencies are 30% and above in both channels, except at low and high m_S , and somewhat lower if the S has a width. The number of data events accepted is 7509 compared with 7210 predicted — an underestimate of about 4% in the simulation, which is rather uniformly distributed at higher masses.

The three-photon channel is characterised by three coplanar deposits of energy in the electromagnetic calorimeter and no charged tracks. Because a Z mediated process is expected to be more isotropic and to have a more uniform distribution of photon energies than the QED background, cuts of $|\cos\theta| < 0.8$ and $E > 3 \text{ GeV}$ were made on all three photons. The sum of the three photon energies was required to be greater than $0.75\sqrt{s}$. There were 57 selected events in the data (with three candidates per event) compared to a Monte Carlo prediction using the generator GGG of 57.8. The signal efficiency is around 50% up to about $87 \text{ GeV}/c^2$ where it drops suddenly because of the photon energy cut.

Energy rescaling was again employed, with significant improvements in resolution. In the e^+e^- and $\mu^+\mu^-$ channels, the branching ratio limit was determined from the invariant mass plot. In the $\gamma\gamma$ channel, where the resolution is about three times worse, and the τ

channel, where the resolution is an order of magnitude worse, the bin edges were moved in 200 MeV steps while maintaining a bin of width 4σ . In the hadronic channel, fits were made to the distribution of E_γ in different dijet invariant mass intervals. The branching ratio limits thus obtained are shown in Fig. 16. The limit for the gg channel is very similar to that for $q\bar{q}$ and is not shown.

Single photon events are the signature of the decay of the scalar into invisible particles, such as a neutrino pair. Events were selected as described in Section 4.2 except that photons were accepted at all energies above 7 GeV. There are 77 events seen in data, while 77.1 are predicted by the radiative neutrino-pair Monte Carlo and 0.3 are predicted by GGG. The signal efficiency is around 60% for all masses up to $70 \text{ GeV}/c^2$, after which it falls slowly to about 50% at $81 \text{ GeV}/c^2$ and then rapidly declines, reaching zero at $84 \text{ GeV}/c^2$. The resolution on the mass recoiling from the photon is around $1 \text{ GeV}/c^2$ at $80 \text{ GeV}/c^2$ but worse than $5 \text{ GeV}/c^2$ below $35 \text{ GeV}/c^2$. There is good agreement between the observed and predicted mass distributions and no signal is observed. The variation of the energy resolution has been taken into account by using variable sized mass bins when deriving the limit on the branching ratio product (Fig. 16).

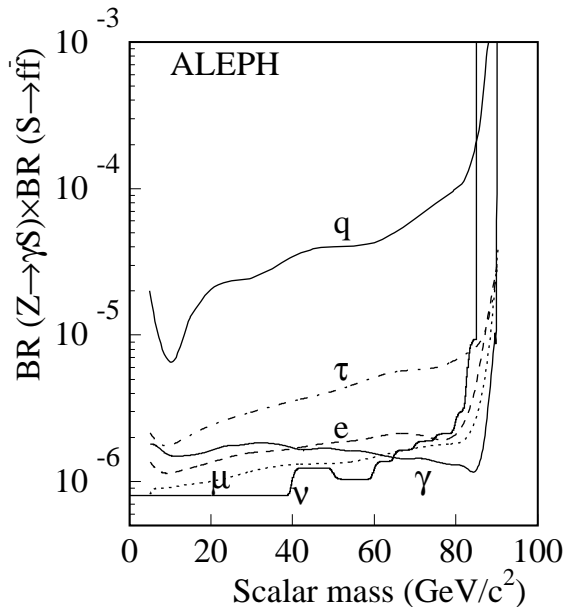


Figure 16: Branching ratio limits at 95% c.l. for scalar production and decay into different final states.

The other LEP collaborations have also published limits on searches for a similar state [45, 51–54].

8 Z decays to three bosons

Anomalous four-boson vertices, leading to the enhancement of branching ratios of Z to three bosons, arise in some composite models. The cross-section is controlled by a compositeness scale factor, Λ , and is proportional to Λ^{-8} . The Standard Model

predictions for the branching ratio for the decays $Z \rightarrow gg\gamma$ and $Z \rightarrow \gamma\gamma\gamma$ are 7.0×10^{-7} and 3×10^{-10} respectively [55] but values in the range 10^{-2} to 10^{-5} have been predicted for some composite models [41]. Variants of analyses reported in previous sections have been used to set branching ratio limits on these decays. A Standard Model signal Monte Carlo was constructed using the JETSET quarkonium to three gluon decay mode, with one or three of the gluons reassigned as a photon as appropriate.

A search for the decay $Z \rightarrow gg\gamma$ was made using a similar analysis to the $q^* \rightarrow q + \gamma$ search, but omitting events containing a single jet and a photon, and with a charge multiplicity cut of four in the hadronic jets. The numbers of data and background Monte Carlo events surviving these cuts were 7350 and 6610 respectively, but the discrepancy is in the region of low photon energy while the Monte Carlo signal is predominantly at high photon energy. The efficiency for the signal Monte Carlo is 46%. The branching ratio limit of 2.8×10^{-5} has been derived from a comparison of the distribution of the cosine of the angle between the hadronic jets as a function of photon energy between the data and the Standard Model prediction. A limit has also been obtained using a matrix element containing composite effects [56] to reweight events from the Standard Model Monte Carlo, but it is not significantly different.

The search for $Z \rightarrow \gamma\gamma\gamma$ was based on the analysis for the channel $Z \rightarrow \gamma S$, $S \rightarrow \gamma\gamma$, excluding events with low energy photons. Cuts were designed to select events with three photons of comparable energy. The lowest photon energy, E_3 , was required to have at least 20% of the beam energy, and the ratio of the energies of the second and third photons was required to be less than 2.4. The low polar angles of the background were exploited by requiring that the lowest energy photon should have a polar angle, θ_3 , satisfying $|\cos \theta_3| \leq (E_3/E_{\text{beam}} + 0.7)/1.2$. The numerical values used in the cuts were optimized using signal and background Monte Carlo events. The signal efficiency is 45% and 42.6 QED events were predicted. As only 41 events were seen, there is no evidence of a signal and a limit is set on the branching ratio $Z \rightarrow \gamma\gamma\gamma$ at 0.50×10^{-5} .

These analyses update the previous ALEPH limits [16] on these branching ratios. Limits have also been published by the other LEP collaborations for $Z \rightarrow \gamma\gamma\gamma$ [57–59] and $Z \rightarrow gg\gamma$ [60].

9 Conclusions

Extensive searches have been made for evidence of compositeness using the full data sample collected by ALEPH at LEP I but no such evidence has been found. The negative outcome of searches for pair production imply mass limits of $m_Z/2$ for excited leptons and quarks with Standard Model coupling to the Z, irrespective of their decay modes. If form factors are assumed at the $Zf^*\bar{f}^*$ vertex then these are typically less than 0.01 for ℓ^* and ν^* and 0.1 for q^* for masses between 10 and 40 GeV/ c^2 . A comprehensive search for weak and radiative decays of excited leptons has enabled limits to be set on couplings for $Z \rightarrow \ell^*\ell$ and $\nu^*\nu$ production which are a significant improvement on earlier measurements for masses up to nearly 90 GeV/ c^2 . No evidence has been found for virtual e^* exchange in the reaction $e^+e^- \rightarrow \gamma\gamma$ and an e^* mass limit of 160 GeV/ c^2 is deduced if the γe^*e coupling is the same as the γee coupling. Coupling limits have been set for single production of excited quarks decaying by either photon or gluon emission. Searches have been made for a scalar partner, S, of the Z in all possible decay modes, for an S mass up

to about $85 \text{ GeV}/c^2$ and branching ratio limits have been presented. Finally, branching ratio limits of 2.8×10^{-5} and 0.50×10^{-5} have been set for the decays $Z \rightarrow gg\gamma$ and $Z \rightarrow \gamma\gamma\gamma$.

Appendix Limits on new processes from electroweak data

Limits on partial widths for new processes can be derived from a comparison of measured electroweak parameters with Standard Model predictions. These can then be used to set coupling limits etc. The procedure was described in detail in a previous ALEPH publication [16] and is updated here. Briefly the experimentally determined values of the total Z width, Γ_Z , the hadronic peak cross-section, σ_h^0 , the hadron to lepton width ratio, R_ℓ [61], are compared to the Standard Model predictions and maximum allowed values of Γ^X , the width of a hypothetical new decay mode $Z \rightarrow X$, determined at 95% confidence level. The Standard Model predictions depend on the top quark mass ($175 \pm 5 \text{ GeV}/c^2$), the Higgs boson mass ($60 < m_H < 1000 \text{ GeV}/c^2$), the strong coupling constant (0.118 ± 0.003), the fine structure constant ($\Delta\alpha^{-1} = 0.12$) and the b quark mass ($\Delta m_b = 0.3 \text{ GeV}/c^2$). Details of the calculation are given in the 1995 CERN Electroweak Working Group Report [62]. Updated values of the input parameters and their errors have been used here to determine a bound (Table 4) on the Standard Model prediction for each observable, taken as one unit of the error from the central value. The allowed interval of a variable was determined assuming a Gaussian measurement error and imposing the Standard Model bound. As an example, for the total width, Γ_Z , the model provides a lower bound of 2483.8 MeV; the area under the Gaussian above the bound is divided in proportion 95:5 and the dividing line gives the position of the upper bound allowed by the measurement error. For the example of Γ_Z this is at 2499.0 MeV, leading to an allowed interval for any new process to contribute to the total Z width of 15.2 MeV. The details of the calculation for each variable are given in Table 4. A lower bound is required for σ_h^0 , while both upper and lower bounds are needed for R_ℓ .

Table 4: Determination of the interval allowed by the Standard Model and consistent with the data at the 95% confidence level.

Variable	Predicted		S.M.	Measured	95% c.l.	Allowed
	value	Error	bound	value	bound	interval
Γ_Z (MeV)	2493.7	9.9	> 2483.8	2494.6 ± 2.7	< 2499.0	15.2
σ_h^0 (nb)	41.471	0.019	< 41.490	41.508 ± 0.056	> 41.391	-0.099
R_ℓ	20.747	0.036	< 20.783	20.788 ± 0.029	> 20.683	-0.100
R_ℓ	20.747	0.036	> 20.711	20.788 ± 0.029	< 20.837	0.126

The relationships between the allowed intervals in Table 4 and partial widths for different event topologies are given in [16]. The limits thus derived are shown in Table 5. The invisible width limit has been derived from the number of neutrino species quoted in Ref. [61] as 2.989 ± 0.012 . These limits have been used in various analyses described in this paper where a direct search was not possible or was inappropriate.

Table 5: Topological width limits from the LEP Z lineshape measurements.

Topology	Origin	Width limit (MeV)	BR limit (%)
any	Γ_Z	15.2	0.61
purely hadronic	Γ_Z	15.2	0.61
non-hadronic	σ_h^0	3.0	0.12
purely leptonic	R_ℓ	1.2	0.05
invisible	N_ν	2.8	0.11

Acknowledgements

We thank our colleagues from the CERN accelerator divisions for the successful operation of LEP. We are indebted to the engineers and technicians at CERN and our home institutes for their contributions to the performance of ALEPH. Those of us from non-member countries thank CERN for its hospitality.

References

- [1] Particle Data Group, Phys. Rev. **D54** (1996) 699.
- [2] N. Cabibbo, L. Maiani and Y. Srivastava, Phys. Lett. **B139** (1984) 459.
- [3] K. Hagiwara, S. Komamiya and D. Zeppenfeld, Z. Phys. **C29** (1985) 115.
- [4] F. Boudjema and A. Djouadi, Phys. Lett. **B240** (1990) 485.
- [5] ALEPH Collab., Nucl. Instr. Meth. **A294** (1990) 121.
- [6] ALEPH Collab., Nucl. Instr. Meth. **A360** (1995) 481.
- [7] ALEPH Collab., Nucl. Instr. Meth. **A346** (1994) 461.
- [8] JADE Collab., Z. Phys. **C33** (1986) 23.
- [9] JADE Collab., Phys. Lett. **B213** (1988) 235.
- [10] A. Courau and P. Kessler, Phys. Rev. **D33** (1986) 2024.
- [11] D. Karlen, Nucl. Phys. **B289** (1987) 23.
- [12] S. Jadach, W. Placzek and B.F.L. Ward, Phys. Lett. **B390** (1997) 298.
- [13] F. Berends and R. Kleiss, Nucl. Phys. **B186** (1981) 22.
- [14] S. Jadach, B. Ward and Z. Wąs, Comput. Phys. Commun. **66** (1991) 276.
- [15] M. Martinez and R. Miquel, Phys. Lett. **B302** (1993) 108.
- [16] ALEPH Collab., Phys. Rep. **216** (1992) 253.

- [17] ALEPH Collab., Phys. Lett. **B385** (1996) 445.
- [18] M. Martinez, R. Miguel and C. Mana, Z. Phys. **C46** (1990) 637.
- [19] F. Berends and P. Davervelt, Nucl. Phys. **B272** (1986) 131.
- [20] F. Berends, R. Kleiss and W. Hollik, Nucl. Phys. **B304** (1988) 712.
- [21] L3 Collab., Phys. Rep. **236** (1993) 1.
- [22] DELPHI Collab., Z. Phys. **C53** (1992) 41.
- [23] L3 Collab., Phys. Lett. **B353** (1995) 136.
- [24] OPAL Collab., Phys. Lett. **B244** (1990) 135.
- [25] OPAL Collab., Phys. Lett. **B257** (1991) 531.
- [26] ALEPH Collab., Phys. Lett. **B384** (1996) 333.
- [27] DELPHI Collab., Phys. Lett. **B380** (1996) 480.
- [28] DELPHI Collab., Phys. Lett. **393** (1997) 245.
- [29] L3 Collab., Phys. Lett. **B384** (1996) 323.
- [30] L3 Collab., Phys. Lett. **B401** (1997) 139.
- [31] OPAL Collab., Phys. Lett. **B377** (1996) 222.
- [32] OPAL Collab., Phys. Lett. **B391** (1997) 197.
- [33] H1 Collab., Nucl. Phys. **B483** (1997) 44.
- [34] ZEUS Collab., Phys. Lett. **B377** (1996) 222.
- [35] F. Boudjema, A. Djouadi and J.L. Kneur, Z. Phys. **C57** (1993) 425.
- [36] T. Sjostrand and M. Bengtsson, Phys. Lett. **B185** (1987) 435.
- [37] V. Barger *et al.* Collider Physics. Frontiers in Physics, (1987).
- [38] F. Podlyski, “Recherche de leptons excités a LEP avec le détecteur ALEPH”. Thèse de l’Université Blaise Pascal, PCCF T 9401, (1994).
- [39] A. Barrès, “Recherche des modes de désintégration hadroniques de leptons excités avec le détecteur ALEPH”. Thèse de l’Université Blaise Pascal, PCCF T 9505, (1995).
- [40] V.F. Obraztsov, Nucl. Instr. Meth. **A316** (1992) 388.
- [41] F. Boudjema and F.M. Renard [convenors]. “Compositeness”. In G. Altarelli *et al.*, editor, *Z Physics at LEP 1*, CERN 89-08, volume 2, 185, (1989).
- [42] F.M. Renard, Phys. Lett. **B132** (1983) 449.

- [43] F.M. Renard, *Nuovo Cim.* **77A** (1983) 1.
- [44] T. Sjostrand and M. Bengtson, *Comput. Phys. Commun.* **43** (1987) 367.
- [45] L3 Collab., *Phys. Lett.* **B292** (1992) 472.
- [46] OPAL Collab., *Phys. Lett.* **B246** (1990) 285.
- [47] CDF Collab., *Phys. Rev. Lett.* **74** (1995) 3538.
- [48] UA2 Collab., *Nucl. Phys.* **B400** (1993) 3.
- [49] F.M. Renard, *Phys. Lett.* **B126** (1983) 59.
- [50] F.A. Behrends and R. Kleiss, *Nucl. Phys.* **B260** (1985) 32.
- [51] L3 Collab., *Phys. Lett.* **B262** (1991) 155.
- [52] DELPHI Collab., *Z. Phys.* **C74** (1997) 577.
- [53] OPAL Collab., *Z. Phys.* **C65** (1995) 47.
- [54] OPAL Collab., *Z. Phys.* **C71** (1996) 1.
- [55] M.L. Laursen, K.O. Mikaelian and M.A. Samuel, *Phys. Rev.* **D23** (1981) 2795.
- [56] F.M. Renard, *Nucl. Phys.* **B196** (1982) 93.
- [57] DELPHI Collab., *Phys. Lett.* **B327** (1994) 386.
- [58] L3 Collab., *Phys. Lett.* **B345** (1995) 609.
- [59] OPAL Collab., *Phys. Lett.* **B257** (1991) 531.
- [60] OPAL Collab., *Phys. Lett.* **B246** (1990) 285.
- [61] The LEP collaborations. A combination of preliminary electroweak measurements and constraints on the Standard Model. CERN-PPE/96-183.
- [62] D. Bardin *et al.* “Electroweak Working Group Report”. In D. Bardin, W. Hollik and G. Passarino, editor, *Reports of the Working Group on precision calculations for the Z resonance*, CERN 95-03, 7, (1995).